

Cite this: *Chem. Soc. Rev.*, 2012, **41**, 8163–8178

www.rsc.org/csr

CRITICAL REVIEW

Applications of extended X-ray absorption fine-structure spectroscopy to studies of bimetallic nanoparticle catalysts†

Anatoly I. Frenkel*

Received 6th May 2012

DOI: 10.1039/c2cs35174a

Extended X-ray absorption fine structure (EXAFS) spectroscopy has been used to study short range order in heterometallic alloys for almost four decades. In this *critical review*, experimental, theoretical and data analytical approaches are revisited to examine their power, and limitations, in studies of bimetallic nanocatalysts. This article covers the basics of EXAFS experiments, data analysis, and modelling of nanoscale clusters. It demonstrates that, in the best case scenario, quantitative information about the nanocatalyst's size, shape, details of core-shell architecture, as well as static and dynamic disorder in metal-metal bond lengths can be obtained. The article also emphasizes the main challenge accompanying such insights: the need to account for the statistical nature of the EXAFS technique, and discusses corrective strategies.

1. Introduction

In the last two decades, there has been a rapid rise in interest in high precision synthesis of bimetallic nanoparticles for catalysis and electrocatalysis.^{1–3} The modification of monometallic supported nanoparticle catalysts with secondary metals is a common strategy for impacting catalyst activity, selectivity, and stability.^{4–7}

Physics Department, Yeshiva University, 245 Lexington Avenue, New York, NY 10016, U.S.A. E-mail: Anatoly.Frenkel@yu.edu; Tel: +1-212-340-7827

† Part of the bimetallic nanocatalysts themed issue.



Anatoly I. Frenkel

Anatoly Frenkel received his MS in Physics from St. Petersburg University and PhD in Physics from Tel Aviv University. He worked as a post-doctoral fellow in the University of Washington and as a research scientist at the University of Illinois at Urbana-Champaign. Since 2001 he has held his present position as a full professor of physics at Yeshiva University. He is also the spokesperson of the Synchrotron Catalysis Consortium at Brookhaven

National Laboratory. He and his colleagues develop new strategies for characterizing nanometer-scale metallic clusters and new operando techniques for studying catalytic reactions. His scientific focus is on studies of structure, dynamics and novel functionalities of disordered materials.

Heterometallic nanoparticles containing platinum group metals are ubiquitous in heterogeneous catalysis. For example, the addition of Re or Ir to a Pt/Al₂O₃ petroleum reforming catalyst significantly enhances its catalytic activity, increases the octane rating of the fuel product, and reduces deactivation of the catalyst due to coking.^{4,8,9}

Bimetallic configurations synthesized to date range in sizes (from 1 to 100 nm), shapes (polyhedral, spherical, nanorods,¹⁰ and tripods^{10,11}), morphologies (octahedral, tetrahedral, cubic^{2,3,10} – some examples are shown in Fig. 1), structures, compositions and types of atomic and compositional ordering (*e.g.*, random, inter-metallic, core-shell,¹² or cluster-on-a-cluster configuration¹⁰).

Many intriguing properties that such configurations display, notably the tuneable electronic properties, synergistic effects, material-specific ensemble effects,¹³ directly affect their activity and/or selectivity.¹⁴ These properties are directly affected by the details of the nanoparticle architecture: the size, composition, uniformity, structure, shape,¹⁵ surface morphology,¹⁶ as well as reaction-driven restructuring.^{14,17} These factors are in

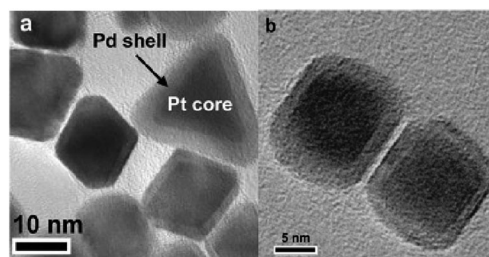


Fig. 1 HRTEM images of Pt (core)–Pd (shell) nanoparticles of different shapes: regular and truncated tetrahedra and octahedra (a), from ref. 3, reprinted with permission from Elsevier, and cubes (b), from ref. 2, reprinted with permission from Elsevier.

the focus of intensive investigation. One of the main challenges in precise, atomistic characterization of the nanocatalyst geometry is the relative difficulty in measuring geometric and compositional details with sufficient spatial resolution. Sensitivity of X-ray diffraction, for example, to the structural details rapidly diminishes as the size of coherent scattering region decreases to a few nm. Even with the spatial resolution (~ 0.5 Å) available in the aberration corrected electron microscopes, such structural characteristics relevant for catalysis as surface strain or lattice contraction (of the order of 0.01–0.1 Å) remain beyond reach of imaging or scattering techniques. Another complication is the limited ability, at the time of writing this review, of even most advanced characterization techniques to perform structural analysis under controlled environmental conditions, *e.g.*, at elevated temperatures and at moderate to high pressure.

X-ray absorption spectroscopy (XAS) and its two main modifications, X-ray Absorption Near Edge Structure (XANES) and Extended X-ray Absorption Fine Structure (EXAFS) are well positioned to bridge this “instrument gap”. XANES, due to its sensitivity to the charge states of metals, adsorbates, and support materials, is a premier tool to study electronic structure of catalytic materials. EXAFS, due to its local structure sensitivity and excellent spatial resolution, is a preferred technique for investigating geometric properties of bimetallic nanocatalysts. Although probing different information, these two methods are part of the same experiment and complement each other in the analysis and interpretation of the results. Experimental and data analysis methods in both techniques have been rapidly developing over the last two decades. In addition to XANES and EXAFS, other inner shell X-ray spectroscopy (*e.g.*, X-ray emission spectroscopy (XES), high energy resolution fluorescence detection (HERFD), resonant inelastic X-ray scattering (RIXS)^{18,19}) and scattering (X-ray diffraction Pair Distribution Function (XRD/PDF)^{20,21} and small angle X-ray scattering (SAXS)²²) techniques have emerged as powerful research methods for bimetallic investigations. In this article we will focus exclusively on the application of EXAFS methods to structural investigations of bimetallic nanocatalysts.

2. Introduction to EXAFS

In this section, we will give a brief overview of the technique. The purpose of this section is to help the reader understand what is the origin of excellent structural, compositional, and dynamic sensitivities, which are essential for studies of metal catalysts. We will also discuss the details of experiment, theory and data analysis methods that help extract relevant information from nanoscale systems, and do so reliably. For extended description into different aspects of XAS methods the readers are referred to the existing review articles, books and book chapters.^{23–28} There are also several recent reviews^{19,29,30} outlining XAS-based applications to structural and catalytic studies of nanoparticles.

At characteristic energies corresponding to the excitation of core-shell electrons X-ray transmission through the sample drops (a portion of X-rays get absorbed by the sample) and the X-ray absorption coefficient $\mu(E)$ exhibits a jump, called X-ray

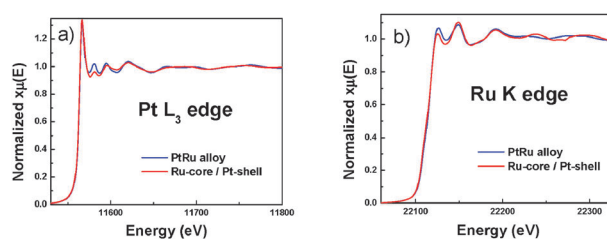


Fig. 2 Raw absorption coefficient data taken on Pt L_3 edge (a) and Ru K edge (b) in Pt Ru alloy and Ru-core–Pt-shell nanoparticles (adapted with permission from ref. 20, Copyright (2009) American Chemical Society).

absorption edge (Fig. 2). The jump is followed by the oscillatory structure, also known as Extended X-ray Absorption Fine Structure, which gave its name to the technique.³¹

The origin of the fine structure that extends through 1000–1500 eV beyond the absorption edge is the interference between the outgoing and incoming photoelectron waves (Fig. 3). The maxima in the extended region in the absorption coefficient correspond to constructive interference, the minima-destructive. The path difference between the two waves is twice the nearest neighbour distance (for the single scattering paths). The EXAFS oscillations are approximately periodic in k -space since the photoelectron wavelength and its wave number are tuned by the incident photon energy:

$k = \sqrt{2m(E - E_0)/\hbar^2}$, where E is the photon energy, and E_0 is the photoelectron energy origin (often chosen either at the middle of the absorption edge jump or at the first inflection point).

These oscillations, resulting from the interference patterns of photoelectrons due to their scattering from neighbouring atoms, contain quantitative information about the local atomic environment in the proximity of the absorbing atom. The frequency of these oscillations is simply a path difference. Therefore, the EXAFS signal contains information about interatomic distances and their disorder (due to the static and dynamic displacements of all atoms from their average positions). The amplitude of the oscillations scales linearly with the number of neighbouring atoms of the same type (Fig. 3a and b). The amplitude and phase of the scattered photoelectron depend also on the type of the scattering element (Fig. 3c). Together, these two sensitivities: to the number, and type, of the nearest neighbour are the most important factors enabling this method to decipher the details of size, structure and composition of bimetallic nanoparticles as described in greater detail below.

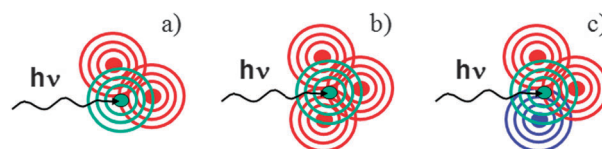


Fig. 3 Schematic of the EXAFS effect: the photoelectron ejected from the X-ray absorbing Pt atom is scattered by different configurations of neighbours: (a) two Pt atoms, (b) three Pt atoms, and (c) two Pt atoms and one Ru atom. These three different configurations give rise to distinct EXAFS signals (as demonstrated also in Fig. 4 and 5).

The oscillatory part of $\mu(E)$, also known as the EXAFS signal, or $\chi(k)$, is obtained by normalizing the $\mu(E)$ by the edge step $\Delta\mu_0(k)$ and subtracting the smooth background function:

$$\chi(k) = \frac{\mu(k) - \mu_0(k)}{\Delta\mu_0(k)}, \quad (1)$$

where $\mu_0(k)$ is a smooth, isolated-atom background function. Examples of background-subtracted, edge-step-normalized EXAFS data are shown in Fig. 4a and b where the sample contained either a core-shell or a random alloy bimetallic Pt/Ru nanoparticles, depending on the details of synthesis.²⁰ It is evident that the EXAFS data can be strongly affected by the geometry and local composition of the nearest environments of both absorbers.

In order to qualitatively examine the structure of an unknown material, often by visually comparing its EXAFS data with a differently treated system or with a reference compound (either pure metal or an alloy of well defined characteristics), it is useful to examine the data in r -space. This can be done by Fourier transforming the $\chi(k)$ EXAFS data. In this process, a weighting factor (either k , or k^2 or k^3) is applied to better emphasize the high k -portion of the data, and a window function is used to minimize Fourier transform artefacts. The so obtained function (Fig. 5) is not equivalent to the pair distribution function of nearest neighbours because of the non-structural components in the EXAFS signal. The most important difference is the shift of the EXAFS Fourier transform peaks to the lower r -values compared to their corresponding interatomic distances. Still, with some experience, it is possible to make a number of qualitative conclusions about structural motifs, and their changes between the samples,

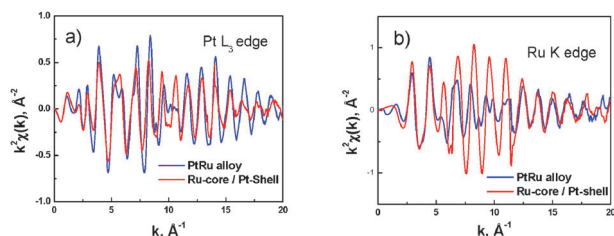


Fig. 4 Edge-step normalized, background-subtracted EXAFS signal $\chi(k)$, weighted with k^2 , for the Pt (a) and Ru (b) edges in the alloy and core-shell bimetallic nanocatalysts supported on γ - Al_2O_3 (adapted with permission from ref. 20, Copyright (2009) American Chemical Society).

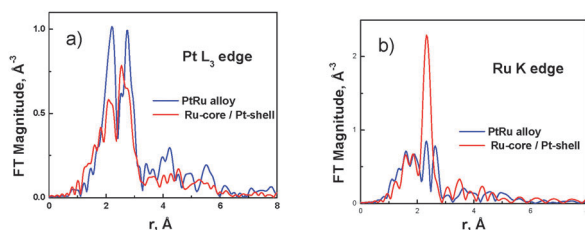


Fig. 5 Fourier transform magnitudes of the k^2 -weighted $\chi(k)$ for the Pt (a) and Ru (b) edges in the alloy and core-shell bimetallic nanocatalysts supported on γ - Al_2O_3 (adapted with permission from ref. 20, Copyright (2009) American Chemical Society).

or in the process of catalytic reaction, from visual examination of the raw data.

2.1 Experiment

XAS experiments are carried out at synchrotron sources that deliver intense (10^{10} photons per s or better) X-ray beams to the sample. In EXAFS experiments, the information about the electronic properties and structural environment of the X-ray absorbing atom and its surroundings is extracted from the X-ray absorption coefficient $\mu(E)$ measured within 1000–1500 eV from the X-ray absorption edge energy. Time-resolved measurements, where a rapid sequence of XANES and/or EXAFS spectra are collected *in situ* or *operando*, in the process of catalytic reaction, are possible either in energy dispersive (DEXAFS)^{32–36} or energy scanning (QEXAFS)^{37–40} modes.

Experiments are performed in a hutch located at the end of the beamline that carries X-ray photons along a tangential path away from the electron storage ring. Since X-ray absorption coefficient is relatively easy to measure (in transmission mode it is accomplished by placing the sample between two X-ray beam detectors for incident and transmitted beams, respectively), this method can be easily adapted to a large number of configurations that may include different sample enclosures (Fig. 6),⁴¹ e.g., a flow cell,^{42,43} a fluid cell,⁴¹ a high pressure reactor,⁴² an electrochemical cell,^{44–47} a fuel cell^{48,49} or a low/high temperature reactor.⁵⁰

As described in greater detail below, a more complete understanding of the structure and catalytic mechanism of a nanoparticle catalyst can be gleaned from combining techniques that examine the same system or process but with different spatial or temporal resolution than any single method. Such combinations include EXAFS and vibrational spectroscopies (IR, UV-Vis and Raman), EXAFS and XRD, all coupled with on-line gas analysis.^{51–55}

In the last decade, in parallel with developing new synchrotron-based methods for studies of nanocatalysts, many new types of research infrastructure were developed as well. Those are organized, managed and funded through research consortia, often at the dedicated beamline facilities. Several synchrotrons have such facilities, among them are X1 beamline at Hasylab at DESY (Germany), X18B (Fig. 7), X19A and X18A beamlines supported by Synchrotron Catalysis Consortium of the NSLS at BNL (US), Swiss-Norwegian beamline at the ESRF (France), SuperXAS at the SLS (Switzerland) and SAMBA beamline at SOLEIL (France).⁵⁶

We will summarize here the uniqueness of EXAFS for catalytic investigations. It can probe local structure with equal facility regardless of the degree of crystallinity and/or dimensionality, of the material, and thus can probe the changes in the structure, from ordered to disordered, or investigate

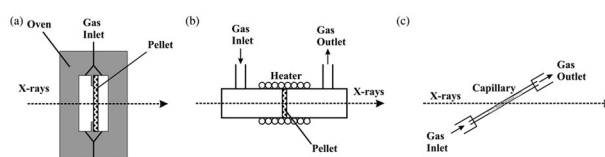


Fig. 6 Different types of *in situ* reactors optimized for XAS experiments: (a), (b) pellet cells and (c) plug flow reactor cell (from ref. 41).

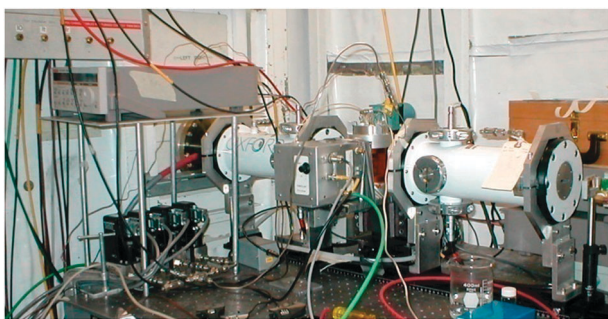


Fig. 7 XAS setup at the X18B beamline at the National Synchrotron Light Source at Brookhaven National Laboratory.

catalyst coarsening, in real time in the process of a reaction. It has excellent element specificity, motivating its use in the studies of bimetallic catalysts or in resolving complex interactions between the catalyst, adsorbates and support. It has long penetration length due to the use of hard X-rays, hence it can easily accommodate reactors for *in situ* and *operando* studies in gas and liquid phases, in an electrochemical or a fuel cell, as well as under high pressure and temperature conditions. High brightness of synchrotron radiation sources enables investigations of low concentrations of real catalysts and high brilliance of third generation synchrotron sources enables spatially resolved XANES and EXAFS measurements using sub-micron X-ray beams. Another important characteristic of synchrotron XAS experiments is the extremely short (10^{-16} – 10^{-15} s) characteristic time of the X-ray absorption effect. Hence, XANES and EXAFS found many applications in time-resolved studies.

2.2 Theory

The EXAFS signal $\chi(k)$ contains the sum of all contributions, $\chi_i(k)$, from groups of neighbors at approximately equal distances from the absorbing atoms (*i.e.*, within the *i*th shell), which are often written as:⁵⁷

$$\chi_i(k) = \frac{S_0^2 n_i}{k R_i^2} |f_i^{\text{eff}}(k)| \sin \left[2k R_i - \frac{4}{3} \sigma_i^{(3)} k^3 + \delta_i(k) \right] \times e^{-2\sigma_i^2 k^2} e^{-2R_i/\lambda_i(k)}, \quad (2)$$

where k is the photoelectron wave number, $f_i^{\text{eff}}(k)$ and $\delta_i(k)$ are the photoelectron scattering-path amplitude and phase, respectively, S_0^2 is the passive electron reduction factor, n_i is the degeneracy of the scattering path, R_i is the effective half-path-length (which equals the interatomic distance for single-scattering paths), σ_i^2 is the mean-square deviation in R_i , $\sigma_i^{(3)}$ is the third cumulant of the pair distribution function,⁵⁸ and $\lambda_i(k)$ is the photoelectron mean free path. The most dominant contribution to the EXAFS signal is from backscattering of the photoelectron by neighboring atoms toward the absorbing atom ("single scattering"). More complex scattering patterns involve the electron wave's reflections off of multiple atoms.²⁶ This multiple scattering approach is essential in order to accurately calculate absorption coefficient. For example, the contribution from multiple scattering by atoms along an atomic row, known as the shadowing or focusing effect, can dominate the backscattering. The amplitude-reduction factor

S_0^2 describes the intrinsic losses upon excitation which arise due to the many body effects in the photoabsorption process.

The scattering amplitudes and phases, along with the photoelectron mean free paths for different scattering configurations contributing to the EXAFS signal (eqn (2)), are calculated *ab initio*. Among the most widely used software programs for these calculations are FEFF (versions 6,⁵⁷ 8⁵⁹ and 9⁶⁰), EXCURVE⁶¹ and GNXAS.⁶²

The σ_i^2 term, also known as EXAFS Debye–Waller factor, reduces the intensity of EXAFS oscillations at high k as a consequence of fluctuations in interatomic distances. It equals the standard deviation in the bond length, caused by configurational (temperature-independent) disorder and dynamic vibrations. Although commonly used in EXAFS analysis as a measure of the bond length disorder, it is applicable only to systems with small to moderate disorder for which the first few terms in the cumulant expansion of the pair distribution function represent it adequately.⁶³ High order cumulants in EXAFS analysis generally describe the asymmetry in the pair distribution function beyond the Gaussian approximation,^{58,64–67} but whether cumulants of order four and higher can be reliably extracted from data is still a debated issue.⁶⁸ Neglecting the anharmonic term (eqn (2)) yields a non-physical decrease in the 1NN bond lengths at high temperatures and can be confused with the *real* negative thermal expansion that has been recently observed in nanoparticles.^{69,70} In order to separate the temperature-independent σ_s^2 and temperature-dependent σ_d^2 , various phenomenological models are often employed, such as the correlated Einstein⁷¹ and correlated Debye⁷² models.

For more details on the theory of EXAFS and different methods of accounting for bond length disorder, the readers are referred to excellent articles and reviews by E. Stern, J. Rehr, G. Bunker, S. Heald, D. Crozier *et al.*^{24,26,27,58,73}

2.3 Data analysis

Methods of data processing and analysis of EXAFS spectra vary significantly, depending on the type of information sought. Among most commonly used methods are nonlinear least square fitting methods,⁷⁴ linear combination analysis^{75–78} and principal component analysis.^{79–82,83} The data analysis can be done by a number of software packages that perform non-linear least square fitting and also report uncertainties in the results. Among the most popular programs based on *ab initio* calculations of X-ray absorption spectra are IFEFFIT,⁸⁴ EXCURVE⁶¹ and GNXAS.⁶²

The EXAFS data processing begins with background subtraction and normalization (eqn (1)). In IFEFFIT data analysis package, this procedure utilizes the AUTOBK code that effectively removes smooth background function by minimizing Fourier components of the signal below the peak corresponding to the first nearest neighbour distance.⁸⁵ To extract structural parameters from the data, the theoretical EXAFS equation (2) must be fit to the measured data. The Levenberg–Marquardt nonlinear least squares algorithm is employed in most commonly used programs. Fitting variables are the structural parameters (*e.g.*, coordination numbers, bond lengths and their disorders). The number of variables should be chosen not to exceed the number of relevant independent data points

in the analysis: $N_{\text{idp}} \approx 2\Delta k\Delta r/\pi$.^{86,87} In this article, most examples shown below utilize the IFEFFIT package that uses Athena and Artemis graphic user interfaces.⁸⁴

3. Coordination numbers in nanoparticles

3.1 Definitions of coordination numbers

The coordination number of the i th shell with the radius R_i (eqn (2)) around the absorbing atom in a monometallic cluster is defined as the average number, per absorber, of nearest neighbours within a given shell:

$$n_{\text{AA}} = \frac{2N_{\text{AA}}}{N_{\text{A}}}. \quad (3)$$

Here N_{AA} is the total number of the A–A nearest neighbors within the same coordination shell, and N_{A} is the total number of A-type atoms in the cluster. The factor of two in eqn (3) is due to the fact that each atom of the A–A pair is an absorber and thus the number of these pairs should be doubled in calculating the A–A coordination numbers.

Analogously, for heterometallic bonds, the coordination number is:

$$n_{\text{AB}} = \frac{N_{\text{AB}}}{N_{\text{A}}}. \quad (4)$$

The information on the homo- and hetero-metallic coordination numbers n_{AA} , n_{AB} , n_{BA} and n_{BB} is available from EXAFS measurements on the absorption edges of both A and B central atoms. The analysis should be done concurrently, with obvious constraints imposed on the heterometallic bonds during the fits:

$$n_{\text{AB}} = \frac{x_{\text{B}}}{x_{\text{A}}} n_{\text{BA}}, \quad (5)$$

$$R_{\text{AB}} = R_{\text{BA}}, \sigma_{\text{AB}}^2 = \sigma_{\text{BA}}^2. \quad (6)$$

A common strategy for analyzing mono- and multi-metallic nanoparticles involves first obtaining the passive electron reduction factor (S_0^2) from a fit to a bulk standard (e.g., metal foil) and then fixing it in the subsequent fits to the nanoparticle data in order to obtain coordination numbers (eqn (2)). Multiple-scattering analysis allows for measurements of coordination numbers within the first 5 shells in the fcc structure in monometallic⁸⁸ and bimetallic⁵⁰ nanoparticles. By measuring coordination numbers, bond lengths and disorder up to the 4–5 coordination shells, the sizes and shapes of nanoparticles as well as their surface morphology and disorder can be analyzed as a function of external conditions such as temperature, gas pressure, alloy composition, and support material.^{88–91}

It is important to stress that it is not always possible to obtain all the desired information (coordination numbers, distances, and disorder factors for each type of atomic pair in the bimetallic nanoalloy) from the data. The reason is the requirement for the number of adjustable parameters P in the fit not to exceed N_{idp} defined above. This criterion can be used at the stage when an EXAFS experiment is planned, to aim at a particular data quality, i.e., the type of signal-to-noise ratio and the values of maximum energy and wavenumber needed for successful analysis of bimetallics. As an illustration, we consider an example of a particular nanoalloy in which we are

interested in the three partial coordination numbers n_{AA} , n_{AB} and n_{BB} (we can use eqn (5) to determine n_{BA}), their respective bond lengths (three values) and their disorders (three more values). To minimize the number of variables we employ the multiple data edge analysis method in this example, where EXAFS data from both edges are analyzed concurrently, by using several constraints (eqn (5) and (6)). Together with the energy origin corrections, unique for each absorption edge, the total number of variables is $P = 11$, i.e., between 5 and 6 per EXAFS spectrum. If we assume that the analysis is to be done for the first shell only, and a typical value for the r -range is between 1.5 and 3 Å (Fig. 5), i.e., $\Delta r = 1.5$ Å, then the k -range should extend from its typical minimum value of 2 Å^{−1} until at least 9 Å^{−1}, i.e., $\Delta k = 7$ Å^{−1}, in order for N_{idp} to be greater than 6: $N_{\text{idp}} = 2 \times 7 \times 1.5/\pi = 6.7$. Since these conditions on the data energy range are quite forgiving, many problems involving real, not model, bimetallic nanoparticles can be solved in a broad range of compositions, temperatures, sample enclosures and *in situ/operando* conditions. When more distant shells (e.g., second through the fourth) are taken into account for more advanced data modeling (see Section 4 for examples), more variables are added to the refinement and, hence, much better data quality is required, where the k -range extends to 15–20 Å^{−1}.

3.2 Using coordination numbers to characterize local compositional motifs

Coordination numbers in bimetallics EXAFS provide critical information pertaining to the compositional habits of bimetallic nanoparticles. For a nanoparticle composed of atoms of type A and B, partial coordination numbers n_{AA} , n_{AB} , n_{BA} and n_{BB} defined above (eqn (3) and (4)) can be measured by multiple-edge refinement of EXAFS data.⁹² These parameters elucidate the intra-particle composition, such as the extent of segregation or alloying of atoms, e.g., random distribution, as opposed to the positive or negative tendency to clustering.^{50,93–101} Once the above parameters are known, the total coordination number of metal–metal (M–M) neighbours per absorbing atom can be found from:⁹⁷

$$n_{\text{MM}} = x_{\text{A}}n_{\text{AM}} + x_{\text{B}}n_{\text{BM}}. \quad (7)$$

The total coordination number can be employed to determine the size and shape using the same methods applied to monometallic particles.

The atoms of the type A will segregate to the surface of the nanoparticle and B to the core, if $n_{\text{AM}} < n_{\text{BM}}$, since atoms at the surface have fewer neighbors than those in the core.⁹⁷ This criterion is useful even for alloys containing elements that are neighbors in the periodic table (e.g., Fe–Ni, Pd–Ag, etc.) where only the total n_{AM} , n_{BM} numbers can be measured by EXAFS analysis of A and B absorbing atoms, respectively, due to the similarity of backscattering amplitudes of A–A and A–B pairs (as well as B–A and B–B).

B. Hwang *et al.*¹⁰² developed a methodology to determine quantitatively the extent of alloying and dispersion in nanoparticles from EXAFS data. Hwang's analysis uses parameters P_{observed} , R_{observed} , P_{random} , and R_{random} where P_{observed} is defined as the ratio of n_{AB} to the total coordination number of metal neighbors to A atoms n_{AM} . R_{observed} is the ratio of n_{BA} to n_{BM} .

P_{random} and R_{random} are the ratios for a perfectly alloyed particle and both have a value of 0.5 if the ratio of the number of A atoms to B atoms is 1 : 1, which implies that $n_{\text{AA}} = n_{\text{AB}}$ and $n_{\text{BB}} = n_{\text{BA}}$. For different ratios of the number of A to B atoms P_{random} and R_{random} are easily determined.⁹⁷ Parameter J_{A} is given by $J_{\text{A}} = \frac{P_{\text{observed}}}{P_{\text{random}}} \times 100\%$ while $J_{\text{B}} = \frac{R_{\text{observed}}}{R_{\text{random}}} \times 100\%$. By contrasting J_{A} and J_{B} to the coordination numbers n_{AA} and n_{BB} the details of the particle composition can be resolved. For example, if $J_{\text{A}} < 100\%$ and $J_{\text{B}} < 100\%$ then A atoms “prefer” being adjacent to A atoms and B atoms “prefer” B atoms, that is, A and B atoms alloy less, indicating a positive tendency for clustering of like atoms. That situation is illustrated in Fig. 8 (right) by two different types of monometallic clusters. If $J_{\text{B}} > J_{\text{A}}$ then the core is A-rich, the shell is B-rich, and $n_{\text{AM}} > n_{\text{BM}}$; whereas if $J_{\text{A}} > J_{\text{B}}$ the core is B-rich, the shell is A-rich, and $n_{\text{BM}} > n_{\text{AM}}$. These core-shell architectures are illustrated in Fig. 8 (left).

A. Frenkel uses a similar characteristic of alloying that is explicitly written in terms of the EXAFS-determined coordination numbers.⁹⁷ For *random* alloys, the average coordination numbers n_{AA} and n_{AB} are in the same proportion as the bulk concentrations of these elements in the sample:⁹⁷

$$\frac{n_{\text{AA}}}{n_{\text{AB}}} = \frac{x_{\text{A}}}{x_{\text{B}}} \quad (8)$$

For alloys with *positive* tendency to clustering of like atoms, *e.g.*, when either the intra-particle or inter-particle segregation is present, the left hand side should be *larger* than the right hand side:

$$\frac{n_{\text{AA}}}{n_{\text{AB}}} > \frac{x_{\text{A}}}{x_{\text{B}}} \quad (9)$$

For homogeneous alloys (Fig. 8, centre) in which the atoms A and B occur with equal probability within the particle or on the surface: $n_{\text{AM}} = n_{\text{BM}}$.⁹⁷ However, even in the homogeneous alloys short range order may be present that can be characterized by Cowley’s short range order parameter:¹⁰³

$$\alpha = 1 - \frac{n_{\text{AB}}/n_{\text{AM}}}{x_{\text{B}}},$$

previously employed for EXAFS studies of bulk alloys.¹⁰⁴ This parameter can be used to investigate the degree of the positive ($\alpha > 0$) or negative ($\alpha < 0$) tendency to clustering within the bimetallic nanoparticles,⁹⁷ where $n_{\text{AM}} = n_{\text{AA}} + n_{\text{AB}}$ is the coordination number of the A-metal bonds. For alloys with positive and negative tendency to clustering, α will be positive or negative, respectively. However, even after the segregation is demonstrated by examining the experimental values of $n_{\text{AA}}/n_{\text{AB}}$ or α , more experimental information is still needed to find out whether A is predominantly in the surface

or in the core, as well as for the determination of the particle size.

The methods of Hwang *et al.* and Frenkel provide a general procedure for quantitatively analyzing atomic distributions. It is important to note that the J_{A} and J_{B} criteria, as defined by Hwang *et al.*, as well as eqn (8) and (9) are meaningful only for sufficiently large clusters and for not too dilute concentrations. We will address this point at greater detail and will generalize this procedure to arbitrary cluster sizes and arbitrary concentrations in the subsequent sections.

4. Examples of analysis of bimetallic configurations

Soon after extended X-ray absorption fine-structure (EXAFS) spectroscopy was first introduced by Stern, Sayers and Lytle as a structural technique,³¹ its potential in solving the structure of heterometallic nanoparticles was recognized by Sinfelt, Via, Meitzner *et al.*^{105–109} Using the ratio method⁵⁸ that relies on extracting the photoelectron amplitude and phase in eqn (2) from experimental standards, or using theoretical calculations by Teo and Lee,¹¹⁰ they built a foundation of the modern methodology of EXAFS analysis and modelling of bimetallic nanoparticles. The level of detail developed in those earlier work is remarkable, given the limitations of the ratio method that can be used for single scattering contributions (and thus the first nearest neighbor analysis) only. For example, Sinfelt *et al.* first recognized the correlations between monometallic and heterometallic coordination numbers that are needed for establishing the surface segregation of Co atoms and the alloy of Co and Os atoms in the core of the Co–Os nanoclusters.¹¹¹ J. Sinfelt in his review describes the use of metal–metal distance for detecting alloying in catalysts, and for quantifying local bimetallic compositions.¹¹² G. Via *et al.* were first to propose the use of eqn (5) for analyzing bimetallic catalysts¹⁰⁹ and to perform simultaneous fits of the EXAFS data collected at each absorption edge of a bimetallic catalyst. G. Sakellson *et al.*¹¹³ were the first to propose the use of eqn (6) for bond length disorder in EXAFS analysis of bimetallics.

These and other^{114–117} advances gave rise to many excellent applications of modern day EXAFS analysis to structural characterization of bimetallic catalysts.^{7,118–127} The following is but a sample of many examples that demonstrate the power of EXAFS analysis of bimetallic nanoparticles using theoretical standards, and advanced data analysis and modelling methods. M. Nashner *et al.*^{50,93} used *in situ* EXAFS to study the nucleation and growth of bimetallic Pt/Ru nanoparticles. Using coordination numbers extracted from multi-edge EXAFS analysis at different temperatures, they established transformation of the starting structure of molecular cluster [PtRu₃]/C precursor toward a transient structure with Pt segregated to the core of the particle. After further reconstruction at higher temperatures, the final structure corresponds to a 1.5 nm average diameter fcc nanoparticle that has a shape of a truncated (by a 111 plane) cuboctahedron (Fig 9). This detailed information was only possible to obtain by first ensuring the high degree of homogeneity, both structural (narrow size distribution, as ascertained by STEM measurements) and compositional

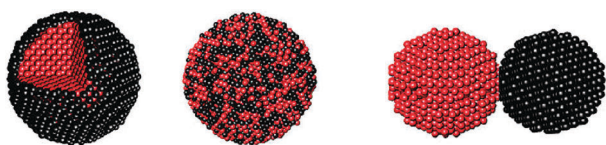


Fig. 8 Three main types of bimetallic configurations: left: core-shell; centre: alloy; right: segregated monometallic clusters (reprinted with permission from ref. 20, Copyright (2009) American Chemical Society).

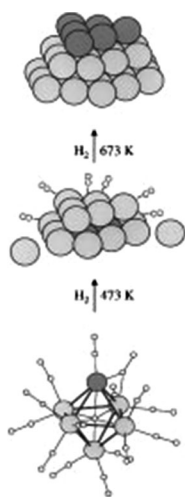


Fig. 9 Schematic of the transformation of incipient Pt–Ru nanoparticles from molecular cluster precursors to a disordered structure at 473 K in which Pt is found preferentially at the core of the condensing particle. After further high-temperature treatment to 673 K, the nanoparticles adopt an inverted structure in which Pt appears preferentially at the surface of the equilibrated bimetallic nanoparticle (reprinted with permission from ref. 93, Copyright (1998) American Chemical Society).

(narrow compositional distribution as ascertained by EDX measurements done in STEM mode)

S. Alayoglu *et al.*²⁰ reported combined, multi-technique investigation of *ca.* 4 nm in size nanoparticles that were synthesized as either alloys, core-shell or separated monometallic clusters (Fig. 8). The raw data of the two types of samples, nominally core-shell and alloy ones, show distinct differences: in the Ru-core/Pt-shell system, Pt appears to have a low *Z* neighbour, Ru EXAFS appears to be metallic in nature. That indicates that Pt segregates to the shell, and Ru to the core in this sample, as expected. The fact that Ru signal is much lower in the multiple-scattering region in the core-shell system compared to the alloy system indicates a high degree of disorder around Ru atoms.

EXAFS data were analyzed concurrently for the Pt L_3 and Ru K-edges (Fig. 10). Best fit results for the coordination numbers (n_1 , n_2 , n_3 and n_4 , for the first through the fourth nearest neighbor coordination shells) were modelled using different structural motifs, fcc (typical for Pt) and hcp (Ru), as well as a common motif (either fcc or hcp) for both elements. The fit results confirmed the conclusions from the visual examination and unique new results about this system. The 4.0 nm Ru@Pt NPs have highly distorted hcp Ru cores that are primarily in the metallic state but show little order beyond 8 Å. In contrast, the 1–2 monolayer thick Pt shells are relatively crystalline but are slightly distorted (compressed) relative to bulk fcc Pt. The homo- and heterometallic coordination numbers and bond lengths are equal to those predicted by the model cluster structure, showing that the Ru and Pt metals remain phase-separated in the core and shell components and that the interface between the core and shell is quite normal. These findings were supported by a combination of TEM, EDS, XANES, PDF and XRD studies.

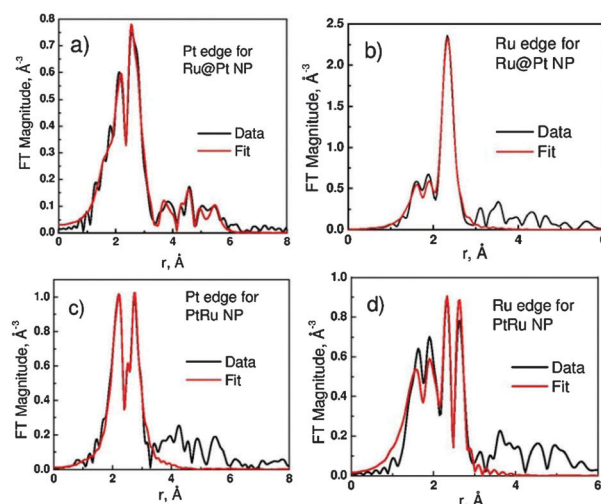


Fig. 10 Fourier transform magnitudes and FEFF6 theory (red) to the EXAFS data at (a) Pt L_3 edge, (b) Ru K-edge for the Ru@Pt core-shell NPs, and at (c) Pt L_3 edge and (d) Ru K-edge for the PtRu 1 : 1 alloy NPs. All NPs were supported on γ - Al_2O_3 (reprinted with permission from ref. 20, Copyright (2009) American Chemical Society).

M. Weir *et al.*⁹⁶ reported synthesis and characterization of bimetallic PdAu dendrimer-encapsulated nanoparticles (DENs). They demonstrated that when 92 Au atoms are reduced onto 55-atom, preformed Pd DEN cores, the two metals invert (Fig. 11). That conclusion was supported by comparing the coordination numbers calculated theoretically: $n_{\text{Au-Au}} = 8.9 \pm 1.0$, $n_{\text{Pd-Au}} = 3.3 \pm 0.8$, and $n_{\text{Pd-Pd}} = 1.0 \pm 2.2$, against the theoretical model corresponding to the inverted configuration (Fig. 11). Theoretical coordination numbers were calculated by a computer program described in ref. 128 that implements the RDF method. Theoretical results were in a good agreement with the experimentally measured coordination numbers, confirming the inversion of the Pd core.

E. Carino *et al.*¹²⁹ reported a two-step process of the Pt core/Cu-shell bimetallic nanoparticle synthesis using underpotential deposition. Due to the instability of Cu monolayers on Pt nanoparticles in air or at the open circuit potential (OCP) in solution, the XAS measurements were performed *in situ*, under potentiostatic control. The coordination numbers of the following 1NN pairs were obtained *via* multiple data set analysis of the Pt L_3 -edge and Cu K-edge measurements: Pt–Pt, Pt–Cu, Cu–Pt, and Cu–Cu. The models calculated by DFT and MD simulations and shown in Fig. 12 were the best match to the experimentally obtained coordination numbers.

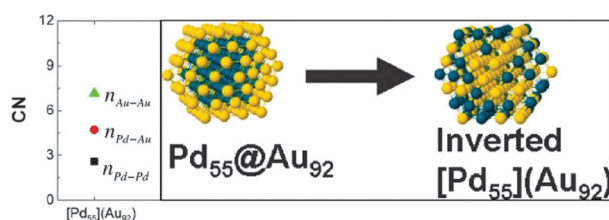


Fig. 11 Model coordination numbers in the inverted $[\text{Pd}_{55}](\text{Au}_{92})$ structure where the core contains 55 Au atoms and the shell – a random alloy of 55 Pd and 37 Au atoms (adapted with permission from ref. 96, Copyright (2010) American Chemical Society).

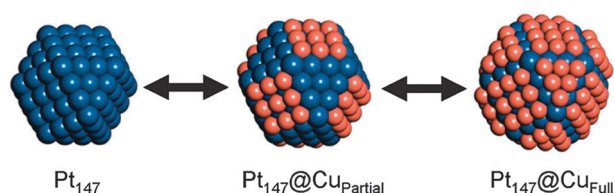


Fig. 12 Two-step process of the underpotential deposition of a Cu-shell onto 1.7 nm Pt nanoparticles synthesized by the dendrimer encapsulation method (reprinted with permission from ref. 129, Copyright (2012) American Chemical Society).

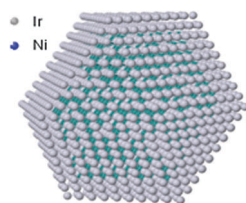


Fig. 13 Atomic configuration of two shell layers of Ir (1454 atoms) on an IrNi alloy core (1030 Ni and 385 Ir atoms), as obtained from EXAFS data modeling (reprinted with permission from ref. 130, Copyright (2011) American Chemical Society).

Even without theoretical refinement using DFT/MD simulations, the best fit results for the coordination numbers unambiguously pointed toward the Pt-rich core and Cu-rich shell.

K. Sasaki *et al.*¹³⁰ synthesized carbon-supported IrNi core-shell nanoparticles. The model shown in Fig. 13 was derived primarily from EXAFS analysis results. EXAFS data at the Ir L₃ edge and Ni K-edge were analyzed to obtain the values, and their ratios, of Ir–Ir, Ir–Ni, Ni–Ni and Ni–Ir coordination numbers. The results were then interpreted using eqn (3)–(5) and (9). It was obtained that the nanoparticle of around 4.7 nm in diameter is composed, on the average, from two-layer Ir shells and IrNi alloy cores. This finding was in excellent agreement with independent STEM observations showing the Ir rich shells. The formation of Ir shell was independently confirmed by time-resolved synchrotron XRD measurements and by STEM observations.

5. How to tell a true core-shell motif from artifacts

In studies of the structure of nanoparticles, coordination numbers are the most important structural parameters that can be obtained from EXAFS analysis. Coordination numbers of the first nearest neighbors (1NN) of X-ray absorbing atoms are obtained by EXAFS analysis very reliably, and are often employed for characterizing nanoclusters in terms of their structure, size, shape and morphology.^{88,90,91,131} Coordination numbers of atomic pairs in bimetallic nanoparticles are often used to discriminate between different types of short range order in the nanoparticles, and/or ascertain the degree of compositional homogeneity in the sample.^{91,97,102} In this section we emphasize the pitfalls in such interpretation when nanoparticle ensembles display a broad range of sizes and compositions. We show the implications of these effects on EXAFS results and describe corrective strategies.

The values of partial coordination numbers are important for analyzing composition habits of heterometallic clusters. For example, depending on the relationship between the partial 1NN numbers and the bulk composition of the nanoalloy, the latter is characterized as either homogeneous (when average environment around each atom is approximately the same) or heterogeneous (when different regions within the sample have different compositional trends, *e.g.*, A-rich and B-rich, or when such segregation occurs within each cluster, *e.g.*, A-rich core and B-rich shell).¹⁰² For homogeneous alloys, relationships (8) and (9) can be used to describe the short range order.⁹⁷ In this section we focus on random nanoalloys (that have zero short range order) and highlight challenges in their detection by EXAFS.

We now introduce the *total* coordination number of metal-metal pairs, or n_{MM} which is equal to n_1 for monometallic clusters. For bulk alloys, when atoms of type A and B are distributed *randomly*, their partial coordination numbers are found from the overall compositions:

$$n_{AA} = n_{BA} = x_A n_{MM}, \quad n_{AB} = n_{BB} = (1 - x_A) n_{MM}, \quad (10)$$

where the composition is defined as: $x_A = N_A/N$. Note that in random bulk alloys, $n_{AA} + n_{BB} = n_{AA} + n_{AB} = n_{BB} + n_{BA} = n_{MM}$.

In a nanocluster with random compositional distribution, more accurate relationships should be used:⁹¹

$$\begin{aligned} n_{AA} &= \frac{N_A - 1}{N - 1} n_{MM} = \frac{N x_A - 1}{N - 1} n_{MM}, \\ n_{AB} &= \frac{N - N_A}{N - 1} n_{MM} = \frac{N}{N - 1} (1 - x_A) n_{MM}, \\ n_{BA} &= \frac{N_A}{N - 1} n_{MM} = \frac{N}{N - 1} x_A n_{MM}, \\ n_{BB} &= \frac{N_B - 1}{N - 1} n_{MM} = \left(1 - \frac{N x_A}{N - 1}\right) n_{MM}. \end{aligned} \quad (11)$$

We note that in random nanoalloys, the same as in the bulk random alloys, $n_{AA} + n_{AB} = n_{BB} + n_{BA} = n_{MM}$ but in the nanoalloys the sum of n_{AA} and n_{BB} is smaller than n_{MM} :

$$n_{AA} + n_{BB} = \frac{N - 2}{N - 1} n_{MM}. \quad (12)$$

Eqn (11) and (12) are exact, and they are equivalent to eqn (3), (4), (8), and (10) in the limit of large total number of atoms (N) and large concentrations (x_A), as demonstrated in Fig. 14.

Furthermore, in the random nanoalloys, the n_{AA} and n_{BB} are different from n_{BA} and n_{AB} , respectively, while in the random bulk alloys they are the same (eqn (10) and (11) and Fig. 15).

We will now investigate how partial coordination numbers are affected by a lack of homogeneity in the sample. The width of compositional distribution over many different clusters may have a large effect on the coordination number measured by EXAFS which is an ensemble averaging method. We assume that within each cluster, atoms of type A and B are distributed randomly, but x_A is different for each nanoparticle. For simplicity, we consider a system that contains particles of the same structure and geometry. Effects of cluster size distribution⁹¹

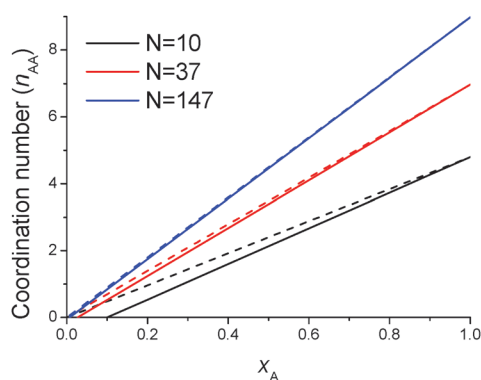


Fig. 14 Exact (solid lines, eqn (11)) and approximate (dashed lines, eqn (10)) behaviours of the coordination numbers of AA pairs for different cluster sizes.

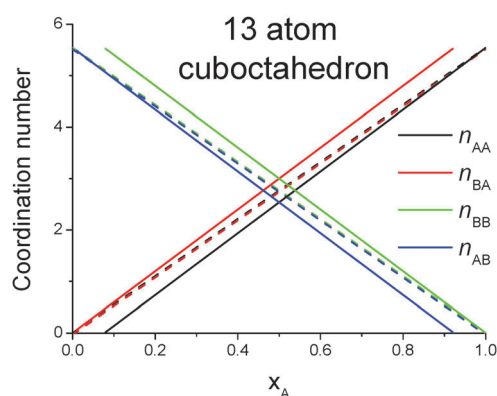


Fig. 15 Coordination numbers of different atomic pairs in random, 13-atom, cuboctahedral alloys. Solid lines correspond to exact calculations using eqn (11) and dashed lines correspond to approximate calculations using eqn (10).

and asymmetric bond length disorder¹³² on the apparent coordination numbers have been described separately.

We distinguish between the particle-specific coordination number n_{AA} (calculated with eqn (11)) in the cluster with the concentration x_A of A atoms, and the *apparent* (measured) coordination number \tilde{n}_{AA} , which, in EXAFS measurement, averages the number of A nearest neighbors over all the A-type atoms in all clusters in the sample. We let the inter-particle compositional distribution of x_A (denoted below as simply x) be a Gaussian with standard deviation σ_c and mean \bar{x} :

$$\rho(x) \propto \exp\left(-\frac{(x - \bar{x})^2}{2\sigma_c^2}\right).$$

In the EXAFS signal, clusters with a greater number of A atoms are weighted more than the clusters with fewer A atoms. We thus write the apparent partial coordination numbers as:

$$\tilde{n}_{AA} = \frac{\int_0^1 \rho(x) n_{AA}(x) dx}{\int_0^1 \rho(x) dx}.$$

Fig. 16 shows the values of \tilde{n}_{AA} and \tilde{n}_{AB} for various values of \bar{x} and σ_c calculated for a cluster containing $N = 100$ atoms. Cluster cartoons are added for clarity. A single cluster

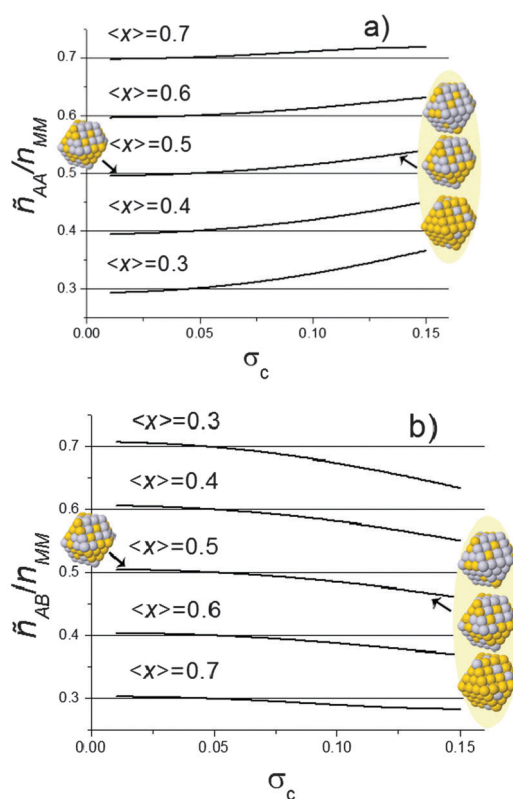


Fig. 16 Normalized partial coordination numbers of (a) AA and (b) AB pairs as functions of the standard deviation σ_c around the average cluster composition $\langle x \rangle$ for clusters of $N = 100$ atoms, calculated assuming a Gaussian compositional distribution. In both figures, cartoons next to the $\langle x \rangle = 0.5$ curve illustrate the difference between the narrow (one cluster on the left) and broad (three different clusters on the right) compositional distributions.

(the cuboctahedral shape was chosen for illustration purpose only) on the left corresponds to narrow inter-cluster compositional distribution (*i.e.*, small σ_c). Three clusters on the right illustrate the change in composition from cluster to cluster (large σ_c). In all cases, the intra-cluster distributions are random.

These results indicate that the ensemble-average coordination numbers \tilde{n}_{AA} can be smaller for narrow compositional distributions or larger for broad distributions than the coordination numbers predicted by the equation $n_{AA} = x n_{MM}$. The reason they are smaller for narrow distributions than the nominal coordination numbers was demonstrated above (eqn (11) and Fig. 15). For broad distributions, the effect is due to the ensemble-averaging that favors A-rich clusters over the B-rich clusters (relative to \bar{x}_A). Similar conclusions can be extended to the other partial coordination numbers. The two sets of values, \tilde{n}_{AA} and n_{AA} , as well as \tilde{n}_{AB} and n_{AB} , agree for $\sigma_c = \sqrt{x(1-x)/N}$, for which the normal distribution coincides with binomial distribution.

In summary, partial coordination numbers in heterometallic nanoparticles can be employed to accurately quantify the intra-particle homogeneity and short-range order for arbitrary cluster sizes and a wide range of component fractions, provided that all the clusters possess nearly identical compositions. If the intra-cluster distribution is completely random but the elemental composition varies widely from cluster to cluster, the coordination

numbers measured by EXAFS will point toward either negative ($\tilde{n}_{AA} < n_{AA}$) or positive ($\tilde{n}_{AA} > n_{AA}$) short range order, which, in the latter case, can be mistaken for a core-shell motif, among other segregation scenarios, even though all clusters are completely random. The only exception when the apparent coordination numbers coincide with those in the “mean” cluster is when the compositional distribution is binomial. With the knowledge of actual compositional distribution (e.g., using energy dispersive X-ray analysis done in electron microscopy experiments) it is possible to correct apparent coordination numbers for the compositional distribution effects (Fig. 16).

6. Complementary techniques

As discussed in the previous section, EXAFS alone cannot be used to characterize size, structure or composition of nanoparticles, without an independent knowledge of their respective distributions, since it is a bulk technique. Many complementary techniques, including catalytic experiments, can be used to characterize bimetallic nanoparticles as demonstrated on several examples below.

Complementary information on the site-specific structure and chemistry can further be obtained using scanning transmission electron microscopy (STEM), which has the unique capability of providing structural and spectral information simultaneously. Supported metal nanoclusters in the size range of 1–100 atoms are ideal for examination using high-angle annular dark field (HAADF) imaging. Correlating the absolute image intensity to the scattering cross-section has been advanced within the STEM-based imaging methods.^{133,134} With this improvement, it is possible to directly count, with accuracy of ± 2 atoms, the number of atoms in a supported nanocluster thus avoiding complexities arising from coherent diffraction. With state of the art electron and X-ray probe methods, one can explore substrate–nanoparticle interactions as a function of the substrate and nanoparticle materials, as well as the size, composition and three-dimensional nanoparticle structure.

J. Batista *et al.*¹³⁵ used a combination of EXAFS, TEM/EDX, and H_2 chemisorption results to demonstrate that the Pd–Cu/ γ - Al_2O_3 catalysts are bimetallic and have nonhomogeneous distribution of both elements. For example, the increase in the Cu : Pd ratio from 1 : 2 to 2 : 1 causes the decrease in hydrogen uptake in the catalysts of approximately the same size (between 1.1 and 0.8 nm) and on the same support. These measurements, coupled with the size determination using TEM and independent EDX studies of compositional distribution, were used to obtain the correlation between the bimetallic architecture and the selectivity in liquid-phase nitrate reduction.

L. Guzzi *et al.*¹³⁶ applied several characterization methods (EXAFS, TPR, XPS and XRD) to study Pt–Co bimetallic catalysts. They analyzed the particle size distribution by XRD and established the absence of particles with large crystallite sizes. Such measurement added confidence to the conclusions derived from their *in situ* EXAFS that the structural results were not biased by the broad distributions in size. The authors addressed also the important question of homogeneity of the

intra-particle composition within the final reduced clusters. While the TEM/EDX was used for this purpose in the previous works of M. Nashner *et al.*⁵⁰ and J. Batista *et al.*¹³⁵ described above, the present authors used TPR for the same purpose. They showed that during reduction with hydrogen, the two families of clusters are formed: the pure Co particles and the Pt–Co particles. We emphasize here that, without such independent measurements, they would not be able to discriminate between the formation of a single alloy Pt:Co phase or a segregation into different types of mono- and bimetallic clusters.

Y. Shu *et al.*¹³⁷ studied the effect of impregnation sequence of γ - Al_2O_3 supported Pt/Ni bimetallic catalysts on their hydrogenation activity and selectivity. The analysis was done only on the Pt L_3 -edge, due to both the low loading of Ni and the possibility of the partial diffusion of Ni into the alumina support. While EXAFS revealed the Pt–Ni bonding in the both types of catalysts, regardless of their impregnation sequence (Ni impregnated first, or Pt impregnated first), EXAFS analysis results were not sufficient for discriminating between different architectural motifs. Thus, the authors used HAADF-STEM imaging that revealed a relatively uniform distribution of the metal particles, with metal particle size ranging between 2 and 3 nm. EXAFS results demonstrated convincingly that the distribution of Pt and Ni within nanoparticles is non-random, regardless of the deposition sequence. In all cases, the n_{Pt-Pt}/n_{Pt-Ni} ratio was found to be greater than the x_{Pt}/x_{Ni} . According to eqn (9), it indicates the segregation of Pt-rich and Ni-rich regions, either within the same particles, or between the particles and the support.

In this work, the catalytic properties of these bimetallic catalysts were used as an additional characterization tool. For example, a significantly higher activity for the disproportionation of cyclohexene and a higher selectivity for the acetylene hydrogenation were found when Pt was impregnated first, when compared with the one where Ni was impregnated first. Co-interpretation of EXAFS and catalytic activity data led to a conclusion that formation of Pt–Ni bimetallic bonds is the key factor affecting catalytic activity for disproportionation of cyclohexene. When Ni was impregnated first, Ni atoms diffused into the cavities of the alumina support, consistent with the fact that no Pt–Ni bonds were observed by EXAFS.

We also note the use of electrochemical methods in nanoparticle surface analysis to complement EXAFS measurements. K. Deplanche *et al.*¹³⁸ studied the structure of Pd–Au nanoparticles prepared by *E. coli* aided synthesis. They used XRD measurements to establish the absence of a significant amount of large crystals. EXAFS analysis was used to confirm the Pd–Au alloy formation and to discern different alloying motifs (random or core-shell-like non-random). The result ($n_{Pd-M} < n_{Au-M}$) allowed them to conclude that Pd atoms are predominantly on the surface of NPs, and Au atoms are predominantly in the core. That conclusion was supported in part by EDX measurement done in STEM mode that demonstrated the bimetallic composition in two randomly chosen nanoparticles (it is recommended that a larger number of particles are investigated, to result in a meaningful compositional distribution). It was also verified by cyclic voltammetry

measurement of surface composition of the nanoparticles, demonstrating a large (compared to the nominal composition) number of Pd surface sites.

7. Overlapping absorption edges

Heterometallic systems containing two or more elements with overlapping absorption edges (*e.g.*, V and Cr, Pt and Ir, Pt and Au, Pt and Re) cannot be simply analyzed by EXAFS since the EXAFS at the higher energy edge overlaps with the EXAFS extending from the lower energy edge. This is a particularly significant problem for metals that neighbour each other in the periodic table such as Re, Ir, Pt, and Au, whose L_3 , L_2 and L_1 absorption edges overlap. In such cases, there is a considerable contribution from the EXAFS of the lower energy element in the spectrum of the higher energy element. Unless these overlapping contributions are disentangled, extracting structural information from the data *via* traditional data analysis strategies is either not possible^{139,140} or difficult and/or insufficiently accurate.¹⁴¹ Indeed, the proximity of the absorption edges in such cases prevents high precision analyses of structure for the lower energy element, while the overlap of their EXAFS signals more generally impedes the interpretation of EXAFS originating from the higher energy element.

The problem of overlapping edges in EXAFS analysis is not limited to heterometallic catalysts, of course. BaTiO₃ is among the most extensively studied perovskites, yet its EXAFS studies are complicated due to the overlap of Ti K-edge and Ba L_3 edge. B. Ravel *et al.* proposed a very original use of diffraction anomalous fine structure (DAFS) technique to deconvolute the EXAFS signals from Ti and Ba.^{142,143} Other methods have appeared recently, based on the use of the high energy resolution fluorescence detection (HERFD) that enabled separation of emission lines from different elements.^{144–147}

L. Menard *et al.* reported a new method for deconvolution of overlapping absorption edges that is based on the use of concurrent, multiple edge analysis of EXAFS data from each edge.¹⁴⁸ The analysis strategy is demonstrated here for an arbitrary bimetallic composition even though, for illustration purpose only, they used notation Ir and Pt for its constituent elements. Data analysis is done by a simultaneous fit of both Ir L_3 and Pt L_3 edges, which involve three contributions: (1) the Ir EXAFS in the Ir L_3 edge before the Pt L_3 edge; (2) the Ir EXAFS in the Pt L_3 edge; and (3) the Pt EXAFS in the Pt L_3 edge. Because (1) and (2) describe the same coordination environments they should be constrained analytically, in the process of fitting each contribution to the experimental data. The analysis is done in *r*-space and is limited to nearest neighbour scattering paths, which are usually well isolated from longer scattering paths in the Fourier transforms of the EXAFS signal $\chi(k)$. In this case, the EXAFS equations that are simultaneously fit are:

$$\chi_{\text{Ir edge}}(k_{\text{Ir}}) = \frac{S_{0,\text{Ir}}^2 N_{\text{Ir}}}{k_{\text{Ir}} R_{\text{Ir}}^2} |f_{\text{Ir}}^{\text{eff}}(k_{\text{Ir}})| \sin \left[2k_{\text{Ir}} R_{\text{Ir}} - \frac{4}{3} \sigma_{\text{Ir}}^{(3)} k_{\text{Ir}}^3 + \delta_{\text{Ir}}(k_{\text{Ir}}) \right] \times e^{-2\sigma_{\text{Ir}}^2 k_{\text{Ir}}^2} e^{-2R_{\text{Ir}}/\lambda_{\text{Ir}}(k_{\text{Ir}})} \quad (13)$$

and

$$\chi_{\text{Pt edge}}(k_{\text{Pt}}, k_{\text{Ir}}) = \frac{S_{0,\text{Pt}}^2 N_{\text{Pt}}}{k_{\text{Pt}} R_{\text{Pt}}^2} |f_{\text{Pt}}^{\text{eff}}(k_{\text{Pt}})| \times \sin \left[2k_{\text{Pt}} R_{\text{Pt}} - \frac{4}{3} \sigma_{\text{Pt}}^{(3)} k_{\text{Pt}}^3 + \delta_{\text{Pt}}(k_{\text{Pt}}) \right] \times e^{-2\sigma_{\text{Pt}}^2 k_{\text{Pt}}^2} e^{-2R_{\text{Pt}}/\lambda_{\text{Pt}}(k_{\text{Pt}})} \quad (14) + \frac{A S_{0,\text{Ir}}^2 N_{\text{Ir}}}{k_{\text{Ir}} R_{\text{Ir}}^2} |f_{\text{Ir}}^{\text{eff}}(k_{\text{Ir}})| \times \sin \left[2k_{\text{Ir}} R_{\text{Ir}} - \frac{4}{3} \sigma_{\text{Ir}}^{(3)} k_{\text{Ir}}^3 + \delta_{\text{Ir}}(k_{\text{Ir}}) \right] \times e^{-2\sigma_{\text{Ir}}^2 k_{\text{Ir}}^2} e^{-2R_{\text{Ir}}/\lambda_{\text{Ir}}(k_{\text{Ir}})}.$$

The factor $A = \Delta\mu_{0,\text{Ir}}/\Delta\mu_{0,\text{Pt}}$, where $\Delta\mu_{0,\text{Ir}}$ and $\Delta\mu_{0,\text{Pt}}$ are the changes in the absorption at the edge steps, is necessary because the extraction of $\chi(k)$ includes a normalization to these edge steps. Therefore, if the Ir L_3 and Pt L_3 edge steps are different in magnitude, the difference in this scaling factor between the Ir EXAFS in the Ir L_3 edge and the Ir EXAFS in the Pt L_3 edge needs to be accounted for. The non-linear least squares fitting of experimental data to eqn (13) and (14) should be done concurrently to the overlapping L_3 edges and can be achieved using available EXAFS analysis tools. In ref. 148, the interface programs Athena and Artemis were used.

Another detail of the analysis is that the Pt EXAFS oscillations as extracted from the experimental absorption edge are described as a function of a single wave vector, k_{Pt} , so the real functional dependence of the data in this range on both k_{Pt} and k_{Ir} , which are referenced to different threshold energies, E_0 , needs to be accounted for. The correction factors $\Delta E_{0,\text{Ir}}$ and $\Delta E_{0,\text{Pt}}$ should be varied for the Ir EXAFS in the Ir L_3 edge and the Pt EXAFS in the Pt L_3 edge, respectively. The correction to the threshold energy (in eV) for the Ir EXAFS in the Pt L_3 edge is then defined as $\Delta E_{0,\text{Ir}} - (349 + \Delta E_{0,\text{Pt}})$, where 349 eV is the difference between the empirical threshold energies, and its purpose is to correct the energy grid in *k*-space for the Ir EXAFS in the Pt L_3 edge. Such a large energy origin shift is necessary in this method since it accounts for a unique $k = 0$ reference point for the Ir EXAFS extending beyond the Pt edge when the Pt edge EXAFS is transformed to *k*-space. The exact value to use (here 349 eV) will depend on the E_0 values that are used in the edge subtraction of the EXAFS spectra. The general rule of thumb that $\Delta E_{0,\text{Ir}}$ and $\Delta E_{0,\text{Pt}}$ should be within the range of *ca.* ± 10 eV to indicate a reasonable theoretical fit is still an appropriate guideline.

In the result of these measures both the Ir and Pt EXAFS data are analyzed over their full energy (or *k*) ranges (with a small gap of $\sim 1.5 \text{ \AA}^{-1}$ centred on the Pt L_3 edge). The ability to carry out a direct fit of the Ir EXAFS that overlaps the Pt L_3 edge significantly minimizes errors in the Pt fitting results. The S_0^2 values required for the analysis are determined from appropriate bulk standards, and A is a constant determined from the absorption edge steps. As such, a total of 10 variables can be used to generate the two-edge fit. This value is well below the information limit of the data. The representative data and fits in *r*-space are shown in Fig. 17. The signature of

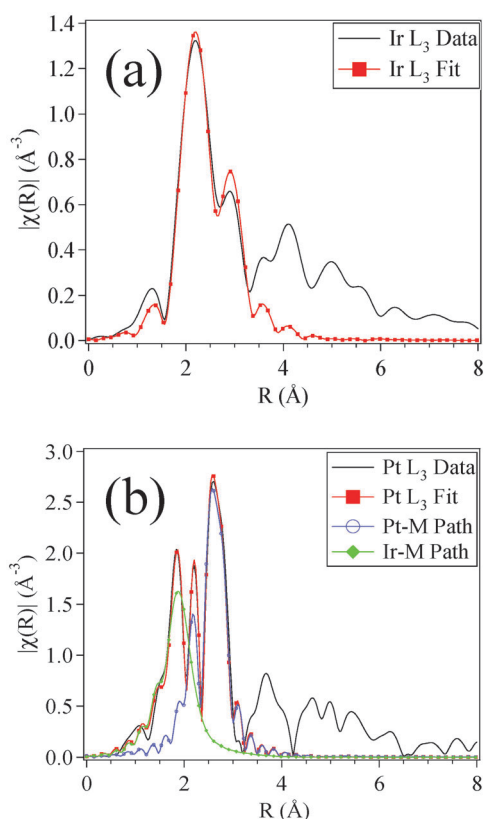


Fig. 17 Comparison of the data and fit of the Ir–Pt nanoparticles on γ - Al_2O_3 under a H_2 atmosphere measured at 215 K at the Ir L_3 and Pt L_3 absorption edges. (a) Fourier transform magnitude of the Ir L_3 data and fit ($k = 2.7\text{--}8.6 \text{ \AA}^{-1}$, $R = 1.2\text{--}3.1 \text{ \AA}$, k^2 -weighted). (b) Fourier transform magnitude of the Pt L_3 data and fit ($k = 2.7\text{--}17.2 \text{ \AA}^{-1}$, $R = 1.3\text{--}3.0 \text{ \AA}$, k^2 -weighted) with the contributions of the individual paths represented (from ref. 148, Copyright (2009) by the American Physical Society).

the Ir L_3 EXAFS “leaking” into the Pt L_3 EXAFS is a low r feature in Fig. 17(b).

8. Heterogeneous mixtures

In this section we will review the case of mixtures. After background subtraction and edge-step normalization of the raw absorption coefficient, resultant EXAFS $\chi(k)$ corresponds to an “average” single atom absorption. The averaging of the local pair distribution functions $\rho(r)$ around all absorbing atoms is obtained automatically in the process of data measurement and reduction: first, the contributions of each absorber’s environments are added by measuring total absorption coefficient, and, at the next stage, are weighted by the molar fractions of absorbing atoms in each species during the edge step normalization:

$$\rho(r) = \sum_{s=1}^n x_s \rho^{(s)}(r), \quad (15)$$

where

$$x_s = \frac{N_s}{N}; \quad \sum_{s=1}^n x_s = 1, \quad (16)$$

In eqn (16), N is the total number of absorbing atoms, n is the total number of species, N_s is the total number of absorbing atoms in species s . Eqn (15) is valid both for the entire r -range of the RDF as well as for the range corresponding to a specific atomic shell within $[r, r + \Delta r]$. Their applications to the coordination numbers of each shell are straightforward:

$$n_{ME_i} = x_s \frac{N_{ME_i}}{N_s} = x_s n_{ME_i}^{(s)}, \quad E_i \neq M, \quad (17)$$

$$n_{MM} = x_s \frac{2N_{MM}}{N_s} = x_s n_{MM}^{(s)}, \quad E_i = M, \quad (18)$$

where N_{ME_i} is the total number of $M\text{--}E_i$ pairs. Note that, since the mixing fractions x_s are constants that contribute to the amplitude of EXAFS equation(2), they correlate only with coordination numbers n_{ME_i} . The nearest neighbor distances R_{ME_i} and their disorders $\sigma_{ME_i}^2$ are calculated the same way for heterogeneous and homogeneous mixtures. Note also that eqn (17) and (18) are a generalization from the case of a homogeneous mixture (where each absorber’s environment is chemically equivalent), in which case $x_s = 1$. Since $n_{ME_i}^{(s)}$ denotes a partial coordination number of $M\text{--}E_i$ within the volume occupied by the species s , it is this parameter that characterizes the local environment of M in this species, not the overall n_{ME_i} measured by EXAFS. For a homogeneous system, $n_{ME_i}^{(s)} = n_{ME_i}$. For a heterogeneous mixture, however, since $N_s < N$, $n_{ME_i}^{(s)} > n_{ME_i}$. Therefore, if the possibility of segregation of the absorbing atoms to chemically different environments is not accounted for in the analysis, the size of the nanoparticles will be underestimated. Since such information is not available from EXAFS, it should be combined with other methods for analysis of heterogeneous systems, as demonstrated below.

8.1 Example 1: dendrimer-encapsulated Pt nanoparticles and unreduced Pt precursors

Consider a common scenario in nanocatalysis where a sample is a mixture of two species: (1) reduced monometallic nanoparticles and (2) molecular precursors, mixed with fractions x_1 and x_2 , respectively. M. Knecht *et al.*¹⁴⁹ described the synthesis and properties of Pt dendrimer-encapsulated nanoparticles (DENs) prepared using sixth-generation, hydroxyl-terminated, PAMAM dendrimers (G6-OH) and three different ratios of the precursors (PtCl_4^{2-}) to dendrimers: 55, 147, and 240. Fig. 18 demonstrates a large fraction of the Pt–low Z bonds to the total coordination of Pt absorbers. That, together with the small Pt–Pt coordination numbers (ranging from 1 to 4 to 6, depending on the precursor to dendrimer ratio), can indicate a very small metal cluster, containing anywhere between 2 to 20 atoms.¹⁵⁰ Combining the EXAFS results with those obtained from UV-vis spectroscopy, X-ray photoelectron spectroscopy, electron microscopy, and high-energy X-ray diffraction it was possible to show that these results are not consistent with a narrow distribution of similar small clusters. A correct model emerged from the combination of all experimental results, one indicating that a relatively small percentage of

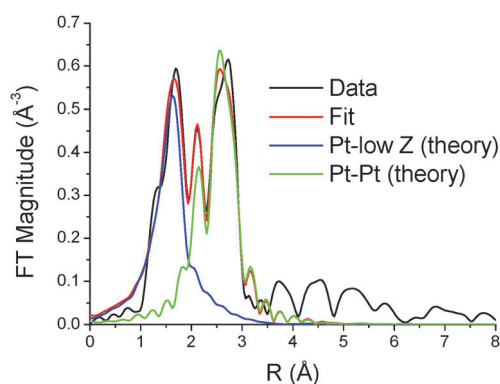


Fig. 18 Fourier transform magnitudes of EXAFS data of Pt L_3 -edge in dendrimer-encapsulated nanoparticles (G6-OH(Pt_{147})), theoretical fit, and individual Pt-low Z and Pt-Pt contributions (adapted with permission from ref. 149, Copyright (2008) American Chemical Society).

the Pt^{2+} /dendrimer precursors are reduced, and the rest remain in the precursor form.

8.2 Example 2: core-shell Ir/Ir-Sn/SnO₂

W. Du *et al.* reported the “surfactant-free” synthesis of carbon supported Ir-Sn alloys with an average diameter of less than 3 nm.¹⁵¹ These systems are potentially important, platinum-free, electrocatalysts for oxygen reduction reaction. The complementary characterization techniques, including aberration-corrected STEM, XRD, XPS, XANES and EXAFS, were used to identify the heterogeneous structure of Ir₇₁Sn₂₉/C particles as Ir/Ir-Sn/SnO₂. The resultant model, consistent with all experimental data, revealed an Ir-rich core, an Ir-Sn alloy shell and SnO₂ regions on the surface. The following description shows the details of the EXAFS analysis. Fig. 19 shows that metallic structures dominate both Ir and Sn in the reduced Ir₇₁Sn₂₉/C (205 °C in the H₂/He flow). The higher resultant Ir-metal (Ir-M) coordination number ($n_{Ir-M} = n_{Ir-Ir} + n_{Ir-Sn} = 9.2 \pm 0.4$) relative to that of Sn-M ($n_{Sn-M} = n_{Sn-Ir} + n_{Sn-Sn} = 4.7 \pm 0.8$) points to the model that has an Ir-rich core and a Sn-rich shell, since such a configuration will cause the Sn environment to be less coordinated by metallic neighbours than the Ir environment, due to the surface truncation effects.⁹⁷ In addition to the Sn-M coordination number being smaller than that of Ir-M, significant Sn-O contribution is an independent evidence for a Sn-rich shell.

By examining partial coordination numbers for Ir-Ir, Ir-Sn, Sn-Ir and Sn-Sn pairs, the authors confirmed this model and further refined it by proposing a more detailed scenario of Ir and Sn segregation. Specifically, they obtained that Ir L_3 -edge EXAFS data are contributed by predominantly monometallic Ir, while the Sn environment is, on the average, heterogeneous: ($n_{Sn-Ir} = 4.2 \pm 0.7$ and $n_{Sn-Sn} = 0.5 \pm 0.4$). This observation further refines their core-shell structure model: the core consists mostly of monoatomic Ir, while the shell is composed of Ir-Sn alloy. The coexistence of the separated SnO₂ and Ir/Ir-Sn nanoparticles can be excluded by the facts that (1) no SnO₂ phase was observed in the XRD pattern and (2) only Ir-core-rich,

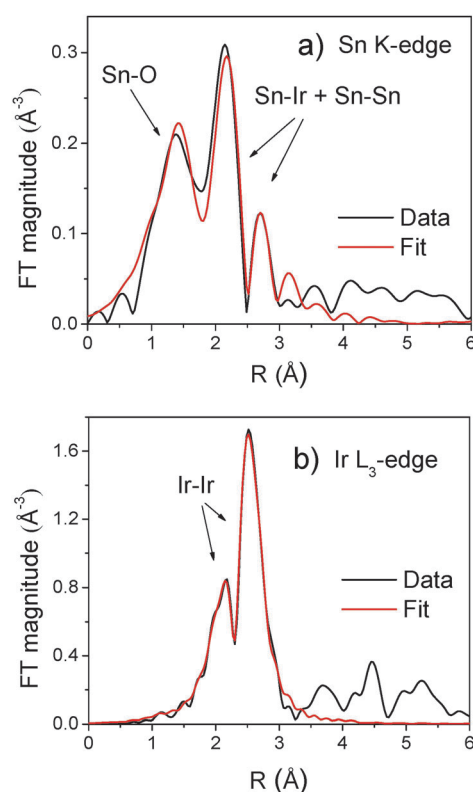


Fig. 19 Fourier transform magnitudes of EXAFS spectra of Ir₇₁Sn₂₉/C sample at Sn K-edge (a) and Ir L_3 edge (b) and their associated fits. The data were collected under a H₂ atmosphere at 205° (adapted with permission from ref. 151, Copyright (2011) American Chemical Society).

Sn-shell-rich structure was observed by STEM-EELS line scans from several individual particles without the observation of separated SnO₂ nanoparticles.

9. Summary and outlook

Many methods and examples shown in this article demonstrate that bimetallic nanoparticles can be analyzed with EXAFS-based methods at very high level of detail, yet reliably, *i.e.*, by accounting for experimental and theoretical uncertainties and artefacts. Recent developments in EXAFS experiment, theory and data analysis helped advance the state of the art in this field from qualitative to quantitative methods. In the past, the catalysts were understood in qualitative terms only: spherical, oblate, raft like, or random, segregated, core-shell, *etc.* Today, we can discriminate between the shapes with particular types of facets, discuss the orientation of a cluster-support interface (*e.g.*, 111 or 001 cubic planes facing the support), attribute the particle shape to a particular polyhedral motif, and claim that a core-shell nanoparticle system may have a random alloy in the core and a particular number of layers in a monometallic shell, to give just a few examples.

This article also attempted to discriminate between the cases when the models and interpretations are unique and reliable, or when alternative explanations of the experimental results are possible. We summarized conditions in which EXAFS

results may offer alternative, and often diametrically opposite interpretations (*e.g.*, (1) random *vs.* non-random alloying of constituting elements, (2) similar particles of approximately the same size, *vs.* a mixture of small and large particles). In these cases, the broad size and compositional distributions are the most notable reasons for arriving at erroneous conclusions. Even in those cases corrective measures can be taken as long as complementary techniques are used, ones that can independently quantify the size and composition heterogeneity in the sample.

In this article, a strong focus was made on the techniques, and tricks, aimed at the increasing accuracy of the coordination number measurements, modelling and interpretation. Today, new methods of synthesis create much better defined model catalysts^{152–155} with much better controlled bimetallic architectures¹⁵³ than decades ago. Continuous development of synchrotron based methods: XES, HERFD¹²³ and RIXS, Modulation Excitation Spectroscopy,¹⁵⁶ XRD/PDF,¹⁵⁷ SAXS and DAFS¹⁵⁸ are adding new opportunities in analyzing bimetallic catalysts by improving energy, spatial and temporal resolutions.

Future X-ray based methods will employ new reactor designs to better study kinetics of chemical reactions, based on microfluidics¹⁴⁷ or nanofluidics¹⁵⁹ technology. New methods of study catalytic reactions in the same conditions by multiple techniques (*e.g.*, XAS and electron microscopy) will emerge, based on new cell designs.¹⁶⁰ Continuous development of focusing optics and new X-ray nanoprobe (currently available at the APS and Diamond, and, in the near future, at the ESRF and NSLS-II) will further bridge the “instrumentation gap” in catalysis science by offering access to single nanoparticles. In these facilities, X-ray spectroscopy, scattering and imaging of individual nanoparticles under *operando* conditions will be possible.¹⁶¹ These experiments will continue to inform, stimulate, and challenge the development of first principle catalysis theories.

Acknowledgements

This work was supported by the U.S. Department of Energy Grant No. DE-FG02-03ER15476.

References

- R. Ghosh Chaudhuri and S. Paria, *Chem. Rev.*, 2011, **112**, 2373–2433.
- N. V. Long, T. Asaka, T. Matsubara and M. Nogami, *Acta Mater.*, 2011, **59**, 2901–2907.
- N. V. Long, T. Duy Hien, T. Asaka, M. Ohtaki and M. Nogami, *Int. J. Hydrogen Energy*, 2011, **36**, 8478–8491.
- Supported Metals in Catalysis*, ed. J. A. Anderson and M. F. Garcia, Imperial College Press, London, 2005.
- L. Guerci, *Catal. Today*, 2005, **101**, 53.
- V. I. Bukhtiyarov and M. G. Slin'ko, *Russ. Chem. Rev.*, 2001, **70**, 147.
- D. Bazin, C. Mottet and G. Tréglia, *Appl. Catal., A*, 2000, **200**, 47–54.
- H. F. Rase, *Handbook of Commercial Catalysts: Heterogeneous Catalysts*, CRC Press, Boca Raton, 2000.
- O. B. Yang, S. I. Woo and Y. G. Kim, *Appl. Catal., A*, 1994, **115**, 229.
- Z. Peng and H. Yang, *Nano Today*, 2009, **4**, 143–164.
- J. Wu and H. Yang, *Nano Res.*, 2011, **4**, 72–82.
- B. D. Yuhas, S. E. Habas, S. C. Fakra and T. Mokari, *ACS Nano*, 2009, **3**, 3369–3376.
- U. B. Demirci, *J. Power Sources*, 2007, **173**, 11–18.
- C. T. Campbell, *Annu. Rev. Phys. Chem.*, 1990, **41**, 775–837.
- Z. L. Wang, T. S. Ahmad and M. A. El-Sayed, *Surf. Sci.*, 1997, **380**, 302–310.
- J. Zhang, M. B. Vukmirovic, Y. Xu, M. Mavrikakis and R. R. Adzic, *Angew. Chem., Int. Ed.*, 2005, **44**, 2132–2135.
- F. Tao, M. E. Grass, Y. Zhang, D. R. Butcher, J. R. Renzas, Z. Liu, J. Y. Chung, B. S. Mun, M. Salmeron and G. A. Somorjai, *Science*, 2008, **322**, 932–934.
- P. Glatzel and U. Bergmann, *Coord. Chem. Rev.*, 2005, **249**, 65–95.
- J. Singh, C. Lamberti and J. A. van Bokhoven, *Chem. Soc. Rev.*, 2010, **39**, 4754–4766.
- S. Alayoglu, P. Zavalij, B. Eichhorn, Q. Wang, A. I. Frenkel and P. Chupas, *ACS Nano*, 2009, **3**, 3127–3137.
- P. J. Chupas, K. W. Chapman, H. Chen and C. P. Grey, *Catal. Today*, 2009, **145**, 213–219.
- R. E. Winans, S. Vajda, B. Lee, S. J. Riley, S. Seifert, G. Y. Tikhonov and N. A. Tomczyk, *J. Phys. Chem. B*, 2004, **108**, 18105–18107.
- E. D. Crozier, *Nucl. Instrum. Methods Phys. Res., Sect. B*, 1997, **133**, 134–144.
- G. Bunker, *A Practical Guide to X-ray Absorption Fine Structure Spectroscopy*, Cambridge University Press, Cambridge, 2010.
- J. E. Penner-Hahn, *Coord. Chem. Rev.*, 1999, **190–192**, 1101–1123.
- J. J. Rehr and R. C. Albers, *Rev. Mod. Phys.*, 2000, **72**, 621–654.
- E. A. Stern and S. M. Heald, in *Handbook of Synchrotron Radiation*, ed. E. E. Koch, North-Holland, 1983, pp. 995–1014.
- H. Wende, *Rep. Prog. Phys.*, 2004, **67**, 2105.
- A. E. Russell and A. Rose, *Chem. Rev.*, 2004, **104**, 4613–4636.
- H. Modrow, *Appl. Spectrosc. Rev.*, 2004, **39**, 183–290.
- D. E. Sayers, E. A. Stern and F. W. Lytle, *Phys. Rev. Lett.*, 1971, **27**, 1204–1207.
- R. P. Phizackerley, Z. U. Rek, G. B. Stephenson, S. D. Conradson, K. O. Hodgson, T. Matsushita and H. Oyanagi, *J. Appl. Crystallogr.*, 1983, **16**, 220–232.
- H. Tolentino, F. Baudelet, E. Dartyge, A. Fontaine, A. Lena and G. Tourillo, *Nucl. Instrum. Methods Phys. Res., Sect. A*, 1990, **289**, 307–316.
- P. G. Allen, S. D. Conradson and J. E. Penner-Hahn, *J. Appl. Crystallogr.*, 1993, **26**, 172–179.
- G. Aquilanti and S. Pascarelli, *J. Phys.: Condens. Matter*, 2005, **17**, 1811.
- O. Mathon, F. Baudelet, J. P. Itié, A. Polian, M. d'Astuto, J. C. Chervin and S. Pascarelli, *Phys. Rev. Lett.*, 2004, **93**, 255503.
- R. Frahm, *Nucl. Instrum. Methods Phys. Res., Sect. A*, 1988, **270**, 578–581.
- M. Richwin, R. Zaeper, D. Lutzenkirchen-Hecht and R. Frahm, *J. Synchrotron Radiat.*, 2001, **8**, 354–356.
- B. S. Clausen, L. Gråbæk, G. Steffensen, P. L. Hansen and H. Topsøe, *Catal. Lett.*, 1993, **20**, 23–36.
- J. M. Lee, N.-E. Sung, J.-K. Park, J.-G. Yoon, J.-H. Kim, M.-H. Choi and K.-B. Lee, *J. Synchrotron Radiat.*, 1998, **5**, 524–526.
- J. D. Grunwaldt, M. Caravati, S. Hannemann and A. Baiker, *Phys. Chem. Chem. Phys.*, 2004, **6**, 3037–3047.
- S. R. Bare, N. Yang, S. D. Kelly, G. E. Mickelson and F. S. Modica, *Catal. Today*, 2007, **126**, 18–26.
- S. R. Bare, G. E. Mickelson, F. S. Modica, A. Z. Ringwelski and N. Yang, *Rev. Sci. Instrum.*, 2006, **77**, 023105.
- J. McBreen, W. E. O'Grady, K. I. Pandya, R. W. Hoffman and D. E. Sayers, *Langmuir*, 1987, **3**, 428–433.
- K. Sasaki, J. Zhang, J. Wang, F. Uribe and R. Adzic, *Res. Chem. Intermed.*, 2006, **32**, 543–559.
- M. G. Weir, V. S. Myers, A. I. Frenkel and R. M. Crooks, *ChemPhysChem*, 2010, **11**, 2942–2950.
- E. M. Erickson, M. S. Thorum, R. Vasić, N. S. Marinković, A. I. Frenkel, A. A. Gewirth and R. G. Nuzzo, *J. Am. Chem. Soc.*, 2011, **134**, 197–200.
- R. Viswanathan, R. Liu and E. S. Smotkin, *Rev. Sci. Instrum.*, 2002, **73**, 2124–2127.
- R. J. K. Wiltshire, C. R. King, A. Rose, P. P. Wells, M. P. Hogarth, D. Thompson and A. E. Russell, *Electrochim. Acta*, 2005, **50**, 5208–5217.

- 50 M. S. Nashner, A. I. Frenkel, D. L. Adler, J. R. Shapley and R. G. Nuzzo, *J. Am. Chem. Soc.*, 1997, **119**, 7760–7771.
- 51 B. M. Weckhuysen, *Chem. Commun.*, 2002, 97–110.
- 52 A. M. Beale, A. M. J. van der Eerden, K. Kervinen, M. A. Newton and B. M. Weckhuysen, *Chem. Commun.*, 2005, 3015–3017.
- 53 N. S. Marinkovic, Q. Wang and A. I. Frenkel, *J. Synchrotron Radiat.*, 2011, **18**, 447–455.
- 54 A. I. Frenkel, Q. Wang, N. Marinkovic, J. G. Chen, L. Barrio, R. Si, A. L. p. Cámara, A. M. Estrella, J. A. Rodriguez and J. C. Hanson, *J. Phys. Chem. C*, 2011, **115**, 17884–17890.
- 55 J.-D. Grunwaldt and A. Baiker, *Phys. Chem. Chem. Phys.*, 2005, **7**, 3526–3539.
- 56 J.-D. Grunwaldt and A. I. Frenkel, *Synchrotron Radiat. News*, 2009, **22**, 2–4.
- 57 S. I. Zabinsky, J. J. Rehr, A. Ankudinov, R. C. Albers and M. J. Eller, *Phys. Rev. B: Condens. Matter Mater. Phys.*, 1995, **52**, 2995–3009.
- 58 G. Bunker, *Nucl. Instrum. Methods*, 1983, **207**, 437–444.
- 59 A. L. Ankudinov, B. Ravel, J. J. Rehr and S. D. Conradson, *Phys. Rev. B: Condens. Matter Mater. Phys.*, 1998, **58**, 7565–7576.
- 60 J. J. Rehr, J. J. Kas, M. P. Prange, A. P. Sorini, Y. Takimoto and F. Vila, *C. R. Phys.*, 2009, **10**, 548–559.
- 61 S. J. Gurman, N. Binsted and I. Ross, *J. Phys. C: Solid State Phys.*, 1984, **17**, 143–151.
- 62 A. Filipponi, A. Di Cicco and C. R. Natoli, *Phys. Rev. B: Condens. Matter Mater. Phys.*, 1995, **52**, 15122–15134.
- 63 E. D. Crozier, J. J. Rehr and R. Ingalls, in *X-ray absorption spectroscopy*, ed. D. C. Koningsberger and R. Prins, John Wiley and Sons, New York, 1988, pp. 373–442.
- 64 J. M. Tranquada and R. Ingalls, *Phys. Rev. B: Condens. Matter Mater. Phys.*, 1983, **28**, 3520–3528.
- 65 H. Kuroda, T. Yokoyama, K. Asakura and Y. Iwasawa, *Faraday Discuss.*, 1991, **92**, 189–198.
- 66 G. Dalba and P. Fornasini, *J. Synchrotron Radiat.*, 1997, **4**, 243–255.
- 67 P. Fornasini, S. A. Beccara, G. Dalba, R. Grisenti, A. Sanson, M. Vaccari and F. Rocca, *Phys. Rev. B: Condens. Matter Mater. Phys.*, 2004, **70**, 174301.
- 68 E. Bus, J. T. Miller, A. J. Kropf, R. Prins and J. A. van Bokhoven, *Phys. Chem. Chem. Phys.*, 2006, **8**, 3248–3258.
- 69 J. H. Kang, L. D. Menard, R. G. Nuzzo and A. I. Frenkel, *J. Am. Chem. Soc.*, 2006, **128**, 12068–12069.
- 70 S. I. Sanchez, L. D. Menard, A. Bram, J. H. Kang, M. W. Small, R. G. Nuzzo and A. I. Frenkel, *J. Am. Chem. Soc.*, 2009, **131**, 7040–7054.
- 71 A. I. Frenkel and J. J. Rehr, *Phys. Rev. B: Condens. Matter Mater. Phys.*, 1993, **48**, 585–588.
- 72 E. Seviliano, H. Meuth and J. J. Rehr, *Phys. Rev. B: Condens. Matter Mater. Phys.*, 1979, **20**, 4908–4911.
- 73 *X-ray Absorption Principles, Applications, Techniques of EXAFS, SEXAFS and XANES*, ed. D. C. Koningsberger and R. Prins, John Wiley & Sons, New York, 1988.
- 74 E. A. Stern, M. Newville, B. Ravel, Y. Yacoby and D. Haskel, *Physica B*, 1995, **208–209**, 117–120.
- 75 J. G. Catalano and G. E. Brown, *Am. Mineral.*, **89**, 1004–1021.
- 76 C. Lamberti, C. Prestipino, F. Bonino, L. Capello, S. Bordiga, G. Spoto, A. Zecchina, S. Diaz Moreno, B. Cremaschi, M. Garilli, A. Marsella, D. Carmello, S. Vidotto and G. Leofanti, *Angew. Chem., Int. Ed.*, 2002, **41**, 2341–2344.
- 77 N. B. Muddada, U. Olsbye, L. Caccialupi, F. Cavani, G. Leofanti, D. Gianolio, S. Bordiga and C. Lamberti, *Phys. Chem. Chem. Phys.*, 2010, **12**, 5605–5618.
- 78 R. Le Toquin, W. Paulus, A. Cousson, C. Prestipino and C. Lamberti, *J. Am. Chem. Soc.*, 2006, **128**, 13161–13174.
- 79 S. R. Wasserman, P. G. Allen, D. K. Shuh, J. J. Rehr and N. M. Edelstein, *J. Synchrotron Radiat.*, 1999, **6**, 284–286.
- 80 S. R. Wasserman, *J. Phys. IV*, 1997, **7**, C2–203–C2–205.
- 81 A. I. Frenkel, O. Kleefeld, S. R. Wasserman and I. Sagi, *J. Chem. Phys.*, 2002, **116**, 9449–9456.
- 82 Q. Wang, J. C. Hanson and A. I. Frenkel, *J. Chem. Phys.*, 2008, **129**, 234502.
- 83 A. Piovano, G. Agostini, A. I. Frenkel, T. Bertier, C. Prestipino, M. Ceretti, W. Paulus and C. Lamberti, *J. Phys. Chem. C*, 2011, **115**, 1311–1322.
- 84 B. Ravel and M. Newville, *J. Synchrotron Radiat.*, 2005, **12**, 537–541.
- 85 M. Newville, P. Liviš, Y. Yacoby, J. J. Rehr and E. A. Stern, *Phys. Rev. B: Condens. Matter Mater. Phys.*, 1993, **47**, 14126–14131.
- 86 L. Brillouin, *Science and Information Theory*, New York, 1962.
- 87 E. A. Stern, *Phys. Rev. B: Condens. Matter Mater. Phys.*, 1993, **48**, 9825–9827.
- 88 A. I. Frenkel, *J. Synchrotron Radiat.*, 1999, **6**, 293–295.
- 89 A. Jentys, *Phys. Chem. Chem. Phys.*, 1999, **1**, 4059–4063.
- 90 A. I. Frenkel, C. W. Hills and R. G. Nuzzo, *J. Phys. Chem. B*, 2001, **105**, 12689–12703.
- 91 A. I. Frenkel, A. Yevick, C. Cooper and R. Vasic, *Annu. Rev. Anal. Chem.*, 2011, **4**, 23–39.
- 92 A. I. Frenkel, E. A. Stern, A. Voronel and S. M. Heald, *Solid State Commun.*, 1996, **99**, 67–71.
- 93 M. S. Nashner, A. I. Frenkel, D. Somerville, C. W. Hills, J. R. Shapley and R. G. Nuzzo, *J. Am. Chem. Soc.*, 1998, **120**, 8093–8101.
- 94 C. W. Hills, M. S. Nashner, A. I. Frenkel, J. R. Shapley and R. G. Nuzzo, *Langmuir*, 1999, **15**, 690–700.
- 95 M. R. Knecht, M. G. Weir, A. I. Frenkel and R. M. Crooks, *Chem. Mater.*, 2008, **20**, 1019–1028.
- 96 M. G. Weir, M. R. Knecht, A. I. Frenkel and R. M. Crooks, *Langmuir*, 2010, **26**, 1137–1146.
- 97 A. Frenkel, *Z. Kristallogr.*, 2007, **222**, 605–611.
- 98 N. Toshima, M. Harada, T. Yonezawa, K. Kushihashi and K. Asakura, *J. Phys. Chem.*, 1991, **95**, 7448–7453.
- 99 N. Toshima and T. Yonezawa, *New J. Chem.*, 1998, **22**, 1179–1201.
- 100 M. Harada, K. Asakura and N. Toshima, *J. Phys. Chem.*, 1994, **98**, 2653–2662.
- 101 K. Asakura, C. R. Bian, S. Suzuki, W. J. Chun, N. Watari, S. Ohnishi, P. Lu and N. Toshima, *Phys. Scr.*, 2005, **T115**, 781–783.
- 102 B. J. Hwang, L. S. Sarma, J. M. Chen, C. H. Chen, S. C. Shih, G. R. Wang, D. G. Liu, J. F. Lee and M. T. Tang, *J. Am. Chem. Soc.*, 2005, **127**, 11140–11145.
- 103 J. M. Cowley, *Phys. Rev.*, 1965, **138**, A1384–A1389.
- 104 A. I. Frenkel, V. S. Machavariani, A. Rubinstein, Y. Rosenberg, A. Voronel and E. A. Stern, *Phys. Rev. B: Condens. Matter Mater. Phys.*, 2000, **62**, 9364–9371.
- 105 F. W. Lytle, G. H. Via and J. Sinfelt, *Erdol Kohle Erdgas Petrochem.*, 1977, **30**, 231.
- 106 J. H. Sinfelt, G. H. Via and F. W. Lytle, *J. Chem. Phys.*, 1978, **68**, 2009–2010.
- 107 G. Meitzner, G. H. Via, F. W. Lytle and J. H. Sinfelt, *J. Chem. Phys.*, 1983, **78**, 882–889.
- 108 G. Meitzner, G. H. Via, F. W. Lytle and J. H. Sinfelt, *J. Chem. Phys.*, 1987, **87**, 6354–6363.
- 109 G. H. Via, K. F. Drake, G. Meitzner, F. W. Lytle and J. H. Sinfelt, *Catal. Lett.*, 1990, **5**, 25–33.
- 110 B.-K. Teo and P. A. Lee, *J. Am. Chem. Soc.*, 1979, **101**, 2815–2832.
- 111 J. H. Sinfelt, G. H. Via, F. W. Lytle and R. B. Gregor, *J. Chem. Phys.*, 1981, **75**, 5527–5537.
- 112 J. H. Sinfelt, *Rev. Mod. Phys.*, 1979, **51**, 569–589.
- 113 S. Sakellson, M. McMillan and G. L. Haller, *Proceedings of AIChE Annual Meeting*, San Francisco, 1984, paper 70g.
- 114 N. Toshima, M. Harada, Y. Yamazaki and K. Asakura, *J. Phys. Chem.*, 1992, **96**, 9927–9933.
- 115 E. Iglesia, S. L. Soled, R. A. Fiato and G. H. Via, *J. Catal.*, 1993, **143**, 345–368.
- 116 A. F. Lee, C. J. Baddeley, C. Hardacre, R. M. Ormerod, R. M. Lambert, G. Schmid and H. West, *J. Phys. Chem.*, 1995, **99**, 6096–6102.
- 117 Y. Wang and N. Toshima, *J. Phys. Chem. B*, 1997, **101**, 5301–5306.
- 118 S. G. Fiddy, M. A. Newton, T. Campbell, J. M. Corker, A. J. Dent, I. Harvey, G. Salvini, S. Turin and J. Evans, *Chem. Commun.*, 2001, 445–446.
- 119 S. H. Choi and J. S. Lee, *J. Catal.*, 1997, **167**, 364–371.
- 120 D. S. Shephard, T. Maschmeyer, B. F. G. Johnson, J. M. Thomas, G. Sankar, D. Ozkaya, W. Zhou, R. D. Oldroyd and R. G. Bell, *Angew. Chem., Int. Ed. Engl.*, 1997, **36**, 2242–2245.

- 121 E. Bus and J. A. van Bokhoven, *J. Phys. Chem. C*, 2007, **111**, 9761–9768.
- 122 O. S. Alexeev and B. C. Gates, *Ind. Eng. Chem. Res.*, 2002, **42**, 1571–1587.
- 123 D. Friebe, D. J. Miller, C. P. O'Grady, T. Anniyev, J. Bargar, U. Bergmann, H. Ogasawara, K. T. Wikfeldt, L. G. M. Pettersson and A. Nilsson, *Phys. Chem. Chem. Phys.*, 2011, **13**, 262–266.
- 124 A. M. Beale and B. M. Weckhuysen, *Phys. Chem. Chem. Phys.*, 2010, **12**, 5562–5574.
- 125 A. M. Molenbroek, S. Haukka and B. S. Clausen, *J. Phys. Chem. B*, 1998, **102**, 10680–10689.
- 126 S. Hannemann, J.-D. Grunwaldt, F. Krumeich, P. Kappen and A. Baiker, *Appl. Surf. Sci.*, 2006, **252**, 7862–7873.
- 127 L. Sciortino, F. Giannici, A. Martorana, A. M. Ruggirello, V. T. Liveri, G. Portale, M. P. Casaletto and A. Longo, *J. Phys. Chem. C*, 2011, **115**, 6360–6366.
- 128 A. I. Frenkel, S. C. Frankel and T. B. Liu, *Phys. Scr.*, 2005, **T115**, 721–723.
- 129 E. V. Carino, H. Y. Kim, G. Henkelman and R. M. Crooks, *J. Am. Chem. Soc.*, 2012, **134**, 4153–4162.
- 130 K. Sasaki, K. A. Kuttijel, L. Barrio, D. Su, A. I. Frenkel, N. Marinkovic, D. Mahajan and R. R. Adzic, *J. Phys. Chem. C*, 2011, **115**, 9894–9902.
- 131 G. Agostini, R. Pellegrini, G. Leofanti, L. Bertinetti, S. Bertarione, E. Groppo, A. Zecchina and C. Lamberti, *J. Phys. Chem. C*, 2009, **113**, 10485–10492.
- 132 A. Yeck and A. I. Frenkel, *Phys. Rev. B: Condens. Matter Mater. Phys.*, 2010, **81**, 115451.
- 133 M. M. J. Treacy and S. B. Rice, *J. Microsc. (Oxford, U. K.)*, 1989, **156**, 211–234.
- 134 A. Singhal, J. C. Yang and J. M. Gibson, *Ultramicroscopy*, 1997, **67**, 191–206.
- 135 J. Batista, A. Pinter, J. P. Gornilšek, A. Kodre and F. Bornette, *Appl. Catal., A*, 2001, **217**, 55–68.
- 136 L. Guzzi, D. Bazin, I. Kovács, L. Borkó, Z. Schay, J. Lynch, P. Parent, C. Lafon, G. Stefler, Z. Koppány and I. Sajó, *Top. Catal.*, 2002, **20**, 129–139.
- 137 Y. Y. Shu, L. E. Murillo, J. P. Bosco, W. Huang, A. I. Frenkel and J. G. Chen, *Appl. Catal., A*, 2008, **339**, 169–179.
- 138 K. Deplanche, M. L. Merroun, M. Casadesus, D. T. Tran, I. P. Mikheenko, J. A. Bennett, J. Zhu, I. P. Jones, G. A. Attard, J. Wood, S. Selenska-Pobell and L. E. Macaskie, *J. R. Soc. Interface*, 2012, 1–8.
- 139 W. R. Flavell, M. Mian, A. J. Roberts, J. F. Howlett, M. M. Sarker, P. L. Wincott, R. L. Bilsborrow and G. van Dorssen, *J. Mater. Chem.*, 1997, **7**, 357.
- 140 C. G. Michel, W. E. Bambrick, R. H. Ebel, G. Larsen and G. L. Haller, *J. Catal.*, 1995, **154**, 222.
- 141 M. Ronning, T. Gjervan, R. Prestvik, D. G. Nicholson and A. Holmen, *J. Catal.*, 2001, **204**, 292–304.
- 142 B. Ravel, C. E. Bouldin, H. Renevier, J.-L. Hodeau and J.-F. Berar, *J. Synchrotron Radiat.*, 1999, **6**, 338–340.
- 143 B. Ravel, C. E. Bouldin, H. Renevier, J. L. Hodeau and J. F. Berar, *Phys. Rev. B: Condens. Matter Mater. Phys.*, 1999, **60**, 778–785.
- 144 M. Hübner, D. Koziej, M. Bauer, N. Barsan, K. Kvashnina, M. D. Rossell, U. Weimar and J.-D. Grunwaldt, *Angew. Chem., Int. Ed.*, 2011, **50**, 2841–2844.
- 145 P. Glatzel, F. M. F. de Groot, O. Manoilova, D. Grandjean, B. M. Weckhuysen, U. Bergmann and R. Barrea, *Phys. Rev. B: Condens. Matter Mater. Phys.*, 2005, **72**, 014117.
- 146 J. Yano, Y. Pushkar, P. Glatzel, A. Lewis, K. Sauer, J. Messinger, U. Bergmann and V. Yachandra, *J. Am. Chem. Soc.*, 2005, **127**, 14974–14975.
- 147 Y. Pushkar, J. Yano, P. Glatzel, J. Messinger, A. Lewis, K. Sauer, U. Bergmann and V. Yachandra, *J. Biol. Chem.*, 2007, **282**, 7198–7208.
- 148 L. D. Menard, Q. Wang, J. H. Kang, A. J. Sealey, G. S. Girolami, X. W. Teng, A. I. Frenkel and R. G. Nuzzo, *Phys. Rev. B: Condens. Matter Mater. Phys.*, 2009, **80**, 064111.
- 149 M. R. Knecht, M. G. Weir, V. S. Myers, W. D. Pyrz, H. C. Ye, V. Petkov, D. J. Buttrey, A. I. Frenkel and R. M. Crooks, *Chem. Mater.*, 2008, **20**, 5218–5228.
- 150 D. Glasner and A. I. Frenkel, *AIP Conf. Proc.*, 2007, **882**, 746–748.
- 151 W. Du, Q. Wang, D. Saxner, N. A. Deskins, D. Su, J. E. Krzanowski, A. I. Frenkel and X. Teng, *J. Am. Chem. Soc.*, 2011, **133**, 15172–15183.
- 152 A. Fukuoaka, H. Araki, Y. Sakamoto, N. Sugimoto, H. Tsukada, Y. Kumai, Y. Akimoto and M. Ichikawa, *Nano Lett.*, 2002, **2**, 793–795.
- 153 S. R. Brankovic, J. X. Wang and R. R. Adžić, *Surf. Sci.*, 2001, **474**, L173–L179.
- 154 B. R. Cuenya, J. R. Croy, S. Mostafa, F. Behafarid, L. Li, Z. F. Zhang, J. C. Yang, Q. Wang and A. I. Frenkel, *J. Am. Chem. Soc.*, 2010, **132**, 8747–8756.
- 155 R. M. Crooks, M. Q. Zhao, L. Sun, V. Chechik and L. K. Yeung, *Acc. Chem. Res.*, 2001, **34**, 181–190.
- 156 D. Ferri, M. S. Kumar, R. Wirz, A. Eyssler, O. Korsak, P. Hug, A. Weidenkaff and M. A. Newton, *Phys. Chem. Chem. Phys.*, 2010, **12**, 5634–5646.
- 157 M. A. Newton, K. W. Chapman, D. Thompson and P. J. Chupas, *J. Am. Chem. Soc.*, 2012, **134**, 5036–5039.
- 158 A. I. Frenkel, A. V. Kolobov, I. K. Robinson, J. O. Cross, Y. Maeda and C. E. Bouldin, *Phys. Rev. Lett.*, 2002, **89**, 285503.
- 159 E. Karabudak, B. L. Mojat, S. Schlautmann, G. Mul and H. J. G. E. Gardeniers, *Anal. Chem.*, 2012, **84**, 3132–3137.
- 160 E. de Smit, I. Swart, J. F. Creemer, G. H. Hoveling, M. K. Gilles, T. Tyliczszak, P. J. Kooyman, H. W. Zandbergen, C. Morin, B. M. Weckhuysen and F. M. F. de Groot, *Nature*, 2008, **456**, 222–225.
- 161 H. Yan, V. Rose, D. Shu, E. Lima, H. C. Kang, R. Conley, C. Liu, N. Jahedi, A. T. Macrander, G. B. Stephenson, M. Nolt, Y. S. Chu, M. Lu and J. Maser, *Opt. Express*, 2011, **19**, 15069.